DESIGN AND MODELLING OF RING RESONATORS: FEASIBILITY STUDY FOR TEMPERATURE SENSORS

A Thesis Submitted to
the Graduate School of
Izmir Institute of Technology
in Partial Fulfillment of the Requirements for the Degree of

MASTER OF SCIENCE

in Electronics and Communication Engineering

by
Aybüke ÖZÇELİK

JULY 2023
IZMIR

We approve the thesis of **Aybüke ÖZÇELİK.**

Examining Committee Members:

Assoc. Prof. Dr. Kıvılcım YÜKSEL ALDOĞAN
Department of Electrical and Electronics Engineering, İzmir Institute of Technology

---
Prof. Dr. Canan VARLIKLI
Department of Photonics, İzmir Institute of Technology

Assist. Prof. Dr. Osman AKIN
Department of Mechatronics Engineering, İzmir Katip Çelebi University

19 July 2023

Assoc. Prof. Dr. Kıvılcım YÜKSEL ALDOĞAN
Supervisor, Department of Electrical and Electronics Engineering
İzmir Institute of Technology

Prof. Dr. Mustafa Aziz ALTINKAYA
Head of the Department of
Electrical and Electronics Engineering

Prof. Dr. Mustafa M. DEMİR
Dean of the Graduate School of
Engineering and Sciences

ACKNOWLEDGEMENTS

ABSTRACT

DESIGN AND MODELLING OF RING RESONATORS: FEASIBILITY STUDY FOR TEMPERATURE SENSORS

Ring resonator structures have garnered significant attention in the field of photonics due to their versatile nature. Temperature can influence the refractive index of the materials used in the resonator, which in turn affects the resonance wavelengths and transmission properties. The purpose of this study was to examine how temperature variations impact the performance of ring resonators. By measuring the resonator response at different temperatures and analyzing the data, it is aimed to understand the thermal behavior of the ring resonators, assess their suitability for practical applications and lays the foundation for further advancements in the design and optimization of ring resonator-based systems.

Within the scope of this thesis, all-pass and add-drop type ring resonators have been produced, and measurements have been carried out at 25 and 35 degrees Celsius. In addition, numerical calculations and simulations of the ring resonators have been performed and compared with experimental data.

ÖZET

HALKA REZONATÖRLERİN TASARIMI VE MODELLENMESİ: SICAKLIK SENSÖRLERİ İÇİN FİZİBİLİTE ÇALIŞMASI

Halka rezonatör yapıları, çok yönlü doğaları nedeniyle fotonik alanında büyük ilgi görmektedir. Sıcaklık, rezonatörde kullanılan malzemelerin kırılma indisi üzerinde etkili olmaktadır, bu da rezonans dalga boylarını ve iletim özelliklerini etkiler. Bu çalışmanın amacı sıcaklık değişimlerinin halka rezonatörlerin performansını nasıl etkilediğini incelemektir. Bu çalışmada, farklı sıcaklıklarda rezanatör tepkisi ölçülerek ve veriler analiz edilerek halka rezanatörlerin termal davranışlarının anlaşılması, pratik uygulamalar için uygunluğunun değerlendirilmesi ve halka rezanatör tabanlı sistemlerin tasasım ve optimizayon konularında temel oluşturulması amaçlanmaktadır.

Bu tez kapsamında, all-pas ve add-drop tipi halka rezonatörler üretilmiş olup ölçümler 25 ve 35 Celsius derecede gerçekleştirilmiştir. Bununla birlikte, halka rezonatörlerin sayısal hesaplamaları ve simülasyonları gerçekleştirilmiş ve deneysel veriler ile karşılaştırılmıştır.

TABLE OF CONTENTS

LIST OF FIGURES

LIST OF TABLES

LIST OF ABBREVATIONS

CMOS…………………………...Complementary Metal Oxide Semiconductor

E……………………………………...…………..Electric Field

F……………………………………….…………...……Finesse

FPGAs…………………………….…………Field Programmable Gate Arrays

FDTD…………………………………….…Finite Difference Element Method

FSR………………………………………..……Free Spectral Range

H………………………………………………………..Magnetic Field

LIDAR……………………………...……………Light Detection and Ranging

MEMS……………………………………....Microelectromechanical Systems

PICs………………………………………….………Photonic Integrated Circuits

Q………………………………………………...…………….Quality Factor

RF……………………………………………….…Radio Frequency

SiPhs……………………………………………….…...Silicon Photonics

SOI……………………………………………………….Silicon-on-Insulators

TE…………………………………………………..Transverse Electric

TM………………………………………….…………Transverse Magnetic

CHAPTER 1

INTRODUCTION

"*Silicon has changed the world through microelectronic technology.*
Now optical researchers are getting in on the silicon game too."

('The lure of silicon', 2007)

1.1.   Silicon Photonics

In traditional bulk optics-based optical systems, the beam is collimated, focused, and transmitted using mirrors, lenses, and prisms. Although lenses refocus the beam, it is refracted and expanded as the beam spreads. Furthermore, bulk optics systems are relatively large and quite sensitive to external influences, and in the event of a barrier in the transmission direction, the beam can be obstructed or dispersed. For these reasons, in many cases, it is more advantageous to transmit light by trapping it in dielectric medium, also known as guided-wave optics, rather than propagate light in free space (Saleh & Teich, 2018).

In the field of guided wave optics, it deals with the propagation and manipulation of light waves through waveguides or optical fibers. Although initially developed for transmitting light over long distances without lenses, guided wave optics has been widely used in various fields that require high data transmission speeds and sensitive detection, ranging from biomedical applications to transportation, a wide range of sensor applications and fiber optic communications.

Integrated optics, also called integrated photonics, is an innovative technology that involves the integration of diverse optical devices and components onto a single substrate which known as chip, resulting in a compact and highly functional optical system. Generating, focusing, splitting, combining, isolating, polarizing, coupling, switching, modulating, and detecting light can be handled by integrated optics.

Photonic integrated circuits (PICs) are a specialized version of electronic integrated circuits, wherein the interconnection between various components is achieved through optical waveguides (Saleh & Teich, 2018). These chips utilize waveguides to enable the integration of different optical devices and components, resulting in a compact and efficient platform for manipulating and controlling light. This technology gets increased attention due to miniaturized chips that integrate multiple optical components onto a single platform, higher speed, and cost-effective solutions.

Even though research on photonic integrated circuits has recently gained popularity, in fact the fields of integrated photonics and integrated electronics emerged simultaneously as well. The first demonstration of a complementary metal oxide semiconductor (CMOS) integrated circuit occurred in 1968, marking the beginning of a significant era. This innovation paved the way for significant improvements in electronics integrated circuits, in line with Moore's law, which asserts that the number of transistors in a densely integrated circuit doubles every two years. In 1969, pioneer paper entitled "Integrated Optics: An Introduction," Stewart Miller demonstrated how photolithographic techniques can be used to fabricate complex circuits. This article is regarded as the start of the field of integrated photonics. Despite starting almost simultaneously, the progress in developing photonic integrated circuits has lagged behind initial expectations when compared to electronics. For a long time, PICs research remained confined to laboratory settings, and the advancements in their development were relatively limited. (Pathak, 2019). The main obstacles to the advancement of photonic integrated circuits can be listed as follows. First of all, in the early years, the absence of applications that would make research, development, and manufacturing investments profitable hindered investments in this field. Another important reason contrasts with integrated electronics, photonic integrated circuits necessitate the integration of a variety of components and materials (Debrégeas-Sillard & Kazmierski, 2008). For instance, different technologies and materials are utilized in various applications. Radio frequency (RF), CMOS or bipolar processes are employed for high-bandwidth electronics, field programmable gate arrays (FPGAs) or high-scaled CMOS are used for digital parts, diffused waveguides on glass are utilized for optical multiplexers and passives, lithium niobate is employed for modulators, and lasers are made of indium phosphide. Additionally, photodetectors and microelectromechanical systems (MEMS)-based switches are based on germanium. These differences cause most photonic components to be produced in limited numbers with different methods in

fabrication facilities, and it is an obstacle for cost effectiveness (Chrostowski & Hochberg, 2019).

Investigations conducted over the past two decades have demonstrated that silicon is an excellent material for building photonic devices as well as suitable for the electronics industry (Hochberg et al., 2013). Silicon photonics (SiPh) is a kind of specialized photonic integrated circuit in which active and passive photonic components and circuits are integrated only on silicon-based materials. The impressive aspect of silicon photonics stems from its ability to integrate numerous functions onto a single chip, leveraging existing microelectronics manufacturing facilities for most of the process (Chrostowski & Hochberg, 2019). Many studies are carried out both in academic and in commercial world in kinds of fields such as communication (Hsu, Nujhat, Kupp, Conley, & Wang, 2023), biosensing (Hu, Sun, Agarwal, & Kimerling, 2009), integrated radio transceivers (Ko et al., 2012), novel light source (Liu et al., 2011), high-speed and microwave signal processing (Burla et al., 2013), light detection and ranging (LIDAR) (Doylend et al., 2011), radio frequency integrated optoelectronics (Burla et al., 2013), nonlinear optics (Foster, Turner, Lipson, & Gaeta, 2008) and many more.

1.2. Ring Resonator

Ring resonator is one of the key components of silicon photonics. In Figure 1, all-pass and add-drop types ring resonator structures illustrate. A standard ring resonator consists of an optical waveguide that forms a loop connected back to itself, in addition to a directional coupler. The loop is in the form of a ring or racetrack shape. Due to its shape and dimension, ring resonator structures can be referred to as micro-ring resonator or racetrack resonator.
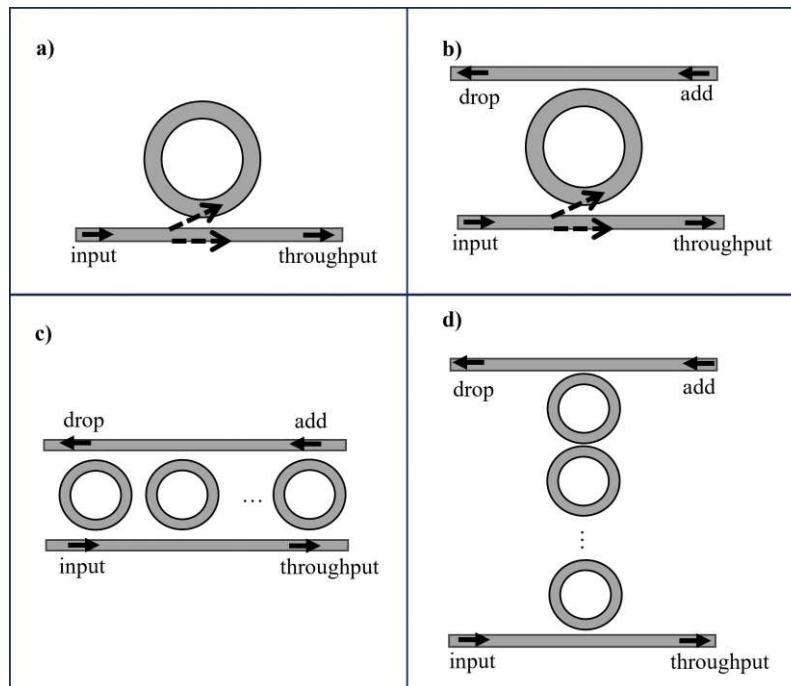
Figure 1. All-pass (a) and add-drop (b) single ring resonators and Serially (c) and parallel (d) cascaded ring resonators (Sources: (Bogaerts, 2011), (Geuzebroek & Driessen, 2006)).

Due to ring structure, resonance occurs in the ring structure when the optical path length of the ring corresponds precisely to a whole number of wavelengths. Ring resonators sustain multiple resonant, the distance between successive resonant wavelength is called free spectral range (FSR). The size of the FSR is determined by the length of the ring. In many applications, a relatively large FSR, typically several nanometers, is desired, necessitating the use of smaller rings. Achieving a compact ring which has a small bend radius is possible only accomplished with high-contrast waveguides that offer strong light confinement (Bogaerts, 2011). In order to remain in the safe zone, however, rings with a radius of less than 5 μm are not recommended. Approximately 20 nm FSR is obtained with a 5-micrometer ring resonator at 1550 nm.

Due to the existence of a limit in reducing resonator dimensions an alternative approach to achieving wider Free Spectral Ranges (FSRs) is by connecting ring resonators with different radius together to form a cascaded ring resonator. In cascade ring resonators, the resonance frequency is equal to the common resonance frequency of

the interconnected rings. As a result, much wider FSRs can be obtained so it paves the way for a wide range of different applications.

Ring resonators possess a straightforward concept and geometry, rendering them adaptable for diverse applications. Microring resonators are versatile optical components that can be basically used as filters (Chen & Lipson, 2009), switches (Biberman et al., 2011), and modulators (Li et al., 2011). Besides, microring resonators can be placed in a series along a common waveguide, with each resonator tuned to a different wavelength. This arrangement makes it possible to perform wavelength-division multiplexing (WDM) efficiently (Lee, Small, Xu, Lipson, & Bergman, 2007). In addition to these, ring resonators find applications in a multitude of different fields: laser tuning (Komljenovic et al., 2017),

Silicon photonic waveguide elements are particularly susceptible to temperature variations because of material properties. Considering the impact of temperature on ring resonator operation is of utmost importance. Precise temperature control, with an accuracy better than 0.1 K, is often necessary to optimize performance. Even slight temperature fluctuations can cause shifts in the device response wavelength, leading to detuning. Besides external temperature changes, self-heating from modulators, lasers, and driver electronics is a significant concern, affecting the performance of photonic devices. Effectively understanding and managing temperature effects are crucial for predicting and adjusting the performance of ring resonators, ensuring reliable outcomes, and facilitating the development of temperature-sensitive applications (Bogaerts, Fiers, & Dumon, 2014).

1.3. State-of-the-Art: Silicon Ring Resonators for Temperature Sensing

When ring resonators first emerged in silicon, their thermal response observed as the shift of resonance wavelengths as illustrated in Figure 2 was a challenge to compensate (Kokubun, Yoneda, & Tanaka, 1996). Later, this feature was exploited for employing them as thermally tunable filters and switches as well as temperature sensors since they provide promising advantages such as low-cost with high-volume fabrication,

immunity to electromagnetic interference, flexible integration with signal-processing electronics, and high sensitivity (Thomson et al., 2016).
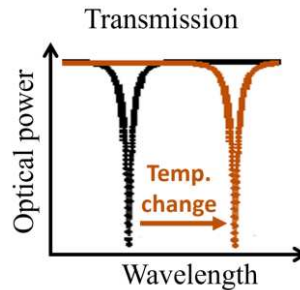
Figure 2. Resonance wavelength shift in the ring resonator due to temperature change

One of the first studies focused on temperature sensing with integrated ring resonator proposed a silicon-nitride-based structure on a metal substrate, which received a sensitivity of 22.5 pm/°C between a relatively wide temperature range that is 25 °C - 350 °C (Zhang & Li,2008). In the same year, an SOI-based ring resonator was used to monitor the temperature of an integrated optical hydrogen detector. The measurements were realized by intensity detection of the transmitted power in the initial resonance wavelength. This approach eliminated the need of optical spectrum analyzer but restricted the sensing range in between 20 and 40 °C (Alam et al.,2008). Two years later, Gun-Duk Kim et al. reported an SOI-integrated-ring-resonator-based temperature sensor and examined the effect of ring resonator parameters on the sensitivity and the device performance. They received the sensitivities of 73 and 83 pm/°C for a waveguide width of 300 and 500 nm, respectively (Kim et al., 2010). In a study conducted by Xu et al. in 2014, a sensitivity of 77 pm/°C was achieved, resulting in a resolution of 1 mK. In order to meet the demands of applications that need better resolution, an approach similar to the one used by Alam was suggested. This method measured the transmitted power intensity on the side of resonance peak, providing a resolution as low as 80 μK. However, the challenge in this approach is the susceptibility to any power fluctuation coming from the light source or environmental conditions (Xu et al., 2014). In 2015, Klimov et.al. studied the zone of stability which describes the optimum structural parameters to minimize the surface scattering and bending loses in the temperature sensing ring

resonator. However, it also imposes a restriction on extending the FSR and sensing range while keeping the high sensitivity (Klimov, Berger, & Ahmed 2015). In 2016, Hyun-Tae Kim and Miao Yu solved this trade-off using cascaded ring resonator configuration which provided a sensitivity of 293.9 pm/°C in a sensing range of 73.48 °C (Kim & Yu, 2016). The mostly studied target temperature range was around the room temperature until You et.al. reported the usage of SOI-based ring resonator in cryogenic temperatures that yielded a sensitivity of 63.9 pm/°C from -93.15 °C to 26.5 °C (You et al., 2020). Besides the ongoing efforts on improving the quality-factor, sensitivity, and sensing range (Lou et al., 2023; Wang et al. 2022) a recent novel design of the cascaded ring resonator with an isolated thermally insensitive reference ring offers self-referenced temperature sensing (Zhu et al. 2023).

1.4.   Objective of this Thesis

This study aims to investigate the impact of temperature variations on the performance of ring resonators. By measuring resonator responses at different temperatures and analyzing the data, the study seeks to understand the thermal behavior of ring resonators, assess their suitability for practical applications, especially temperature sensors, and lay the foundation for future advancements in designing and optimizing ring resonator-based systems.

The thesis is organized as follows: Chapter 2 involves the fundamentals of silicon-on-insulator, optical waveguides, directional couplers, and ring resonators. In Chapter 3, the numerical method employed in this study, the fabrication and measurement system, and the methodologies used for analyzing theoretical and experimental data are explained. In Chapter 4, comparative analyses are conducted between the theoretical data and the experimental data and discussed. In Chapter 5, a summary of the thesis is presented with the future work.

CHAPTER 2

BACKGROUND INFORMATION

Photonic integrated circuits are formed by the simultaneous operation of many subcomponents. This section covers the components used in a ring resonator system.

2.1. Silicon-on-Insulators

Silicon-on-insulators (SOI) are wafers commonly used in integrated photonic devices. There are three main reasons why SOIs are widely used in integrated photonics. First of all, it provides the high refractive index contrast for the light propagation in the waveguide. Secondly, the low absorption of crystalline silicon at wavelengths longer than 1200 nm which also include telecom wavelengths such as 1310 and 1550 nm in this region have made SOIs preferable. Finally, SOI is compatible with CMOS manufacturing processes. Thus, production can be carried out using the CMOS infrastructure (Bogaerts & Selvaraja, 2014).
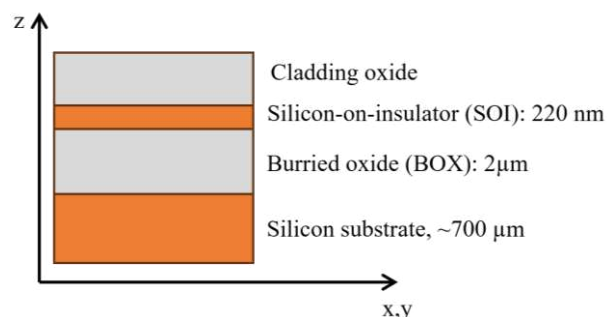
Figure 3. Cross sectional view of SOI wafer (Source: (Chrostowski & Hochberg, 2019)).

Although it should be noted that there is no standard for an SOI structure, typical preferred materials and thicknesses are as in Figure 3. 700 mm thick silicon substrate forms the bottom layer of a wafer. The middle layer consists of 2 µm thickness buried oxide and on top of wafer there is crystalline silicon with a thickness of 220 nm. Finally, SOI wafer is covered with a cladding oxide layer (Chrostowski & Hochberg, 2019).

2.1.1. Silicon

2.1.1.1. Wavelength Dependence of Silicon
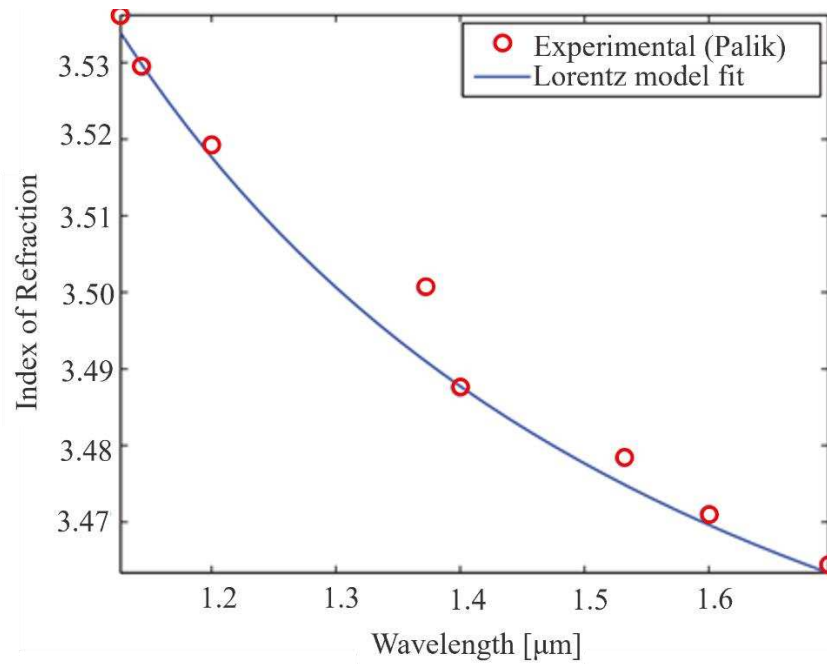
Figure 4. Silicon refractive index 300 K (Source:(Chrostowski & Hochberg, 2019)).

The refractive index of the silicon defines how light will propagate through the silicon. This phenomenon is called dispersion. The refractive index can be expressed as a function of wavelength. One of the methods which can be used to calculate the refractive index is the Lorentz model in Equation 2.1. and the effective index change according to the wavelength is illustrated in Figure 4.

$$n^2(\lambda) = \varepsilon + \frac{\varepsilon_{Lorentz} \, \omega_0{}^2}{\omega_0{}^2 - 2i\delta_0 \frac{2\pi c}{\lambda} - \left(\frac{2\pi c}{\lambda}\right)^2} \tag{2.1}$$

where $\varepsilon = 7.9874$, $\varepsilon_{Lorentz} = 3.6880$, $\omega_0 = 3.9328 \, x \, 10^{15}$ and $\delta_0 = 0$ at the wavelentg between 1150 nm to 1800 nm according to Palik's handbook (Palik, 1998), (Chrostowski & Hochberg, 2019).

2.1.1.2. Thermo-optic Effect in Silicon

The temperature-induced shrinkage of the bandgap, changes in the distribution of carriers and phonons, and the thermal expansion of the crystal with varying temperature collectively give rise to the thermo-optical effect. This effect, known as the thermo-optical effect, leads to modifications in the refractive index at a constant pressure and remains a subject of considerable academic and scientific interest, particularly in the domains of optics and photonics. (Pavesi & Guillot, 2006). The thermo-optic effect is expressed by the change of n as a function of temperature. The thermo-optic coefficient of silicon at a wavelength of 1550 nm is measured $1.87 \, x \, 10^{-4} \, \text{K}^{-1}$ (Frey & Leviton, 2006).

2.1.2. Silicon Dioxide

Silicon dioxide demonstrates a lower refractive index when compared to silicon, leading to effective light confinement within the silicon waveguide. Notably, the temperature-dependence of silicon dioxide's refractive index is approximately 6.3 times lower than that of silicon. This characteristic renders silicon dioxide a good choice for diverse applications, particularly in scenarios where maintaining stable optical properties under varying temperature conditions is of paramount importance. (Dumon, 2007). Figure 5 shows the refractive index change according to the wavelength.
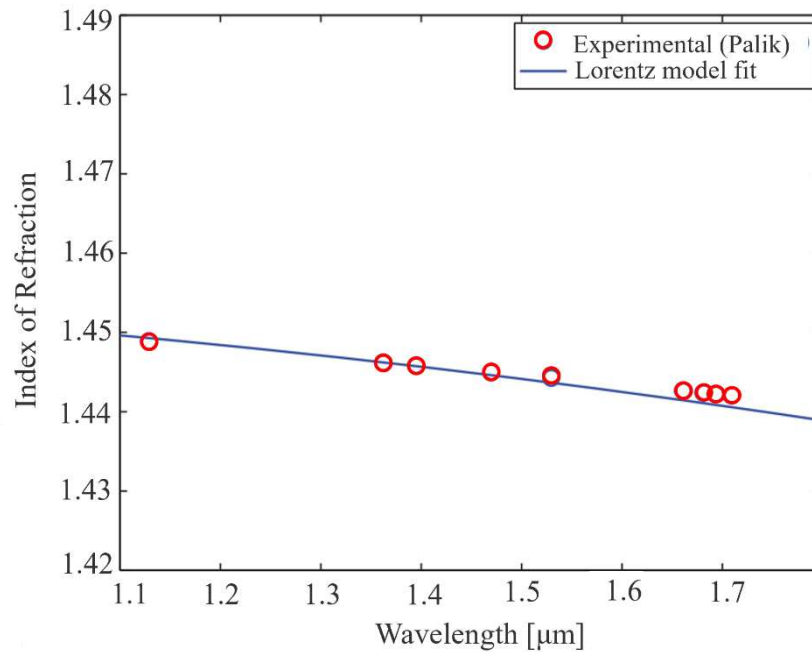
Figure 5. Silicon dioxide refractive index 300 K (Source:(Chrostowski & Hochberg, 2019)).

2.2.   Optical Waveguides

Waveguides constitute the fundamental elements of photonic devices and systems. By minimizing light dispersion and loss, it confines and guides light along desired paths routes. As a result, optical waveguides connect various PIC building pieces to enable the transmission of optical signals.

Ray optics can explain the confinement and propagation of light on optical waveguides. Optical waveguides are composed of dielectric materials with a high index of refraction. Since light cannot pass into a medium with a lower refractive index at the boundary of the waveguide, it is reflected at the angle from which it originated, according to the principle of total internal reflection. Along the path, light is reflected, and redirected along the path. The light is said to be confined in the waveguide because it propagates by reflecting along the waveguide. It should be noted that this is an ideal situation some optical power tunnels. The term for this wave outside the waveguide is evanescent wave (Khare, 2004).

2.2.1. Optical Mode

Although the ray approach brings an explanation to the confinement in the waveguide, it is not sufficient to understand the wave behavior of light. Since the dimension of the waveguide is comparable to the wavelength, the propagation of light in the waveguide can be explained by a more comprehensive approach which is called Electromagnetic Optics. In electromagnetic optics, the electromagnetic field is defined as the position and time-dependent function of the electric field $E(r, t)$ and the magnetic field $\mathcal{H}(r, t)$ with respect to position and time. The relationship between those fields is governed by the following Maxwell's equations for electromagnetic fields in a dielectric medium.

$$\nabla \ x \ \mathcal{H} \ = \ \varepsilon \frac{\partial E}{\partial t}, \tag{2.2}$$

$$\nabla \ x \ E \ = \ -\mu \frac{\partial \mathcal{H}}{\partial t}, \tag{2.3}$$

$$\nabla . \, \mathcal{E} = 0 \,, \tag{2.4}$$

$$\nabla . \, \mathcal{H} = 0 \,, \tag{2.5}$$

where ε and μ represent electric permittivity and magnetic permittivity, respectively.

Each constituent of the electric field and magnetic field satisfies the following wave equation.

$$\nabla^2 u - \frac{1}{v^2}\frac{\partial^2 u}{\partial t^2} = 0 \qquad (2.6)$$

where v is the speed of the light in the medium which is given by (Saleh & Teich, 2018):

$$v = \frac{1}{\sqrt{\varepsilon\mu}}. \qquad (2.7)$$

Maxwell Equations can be solved for two different polarizations in rectangular waveguides. Two scenarios arise from geometry: either the electric field (E) or the magnetic field (H) is parallel to the layer interfaces. These scenarios define T transverse electric (TE) or transverse magnetic (TM) polarizations in the direction of light propagation.

The general form of electromagnetic radiation can be represented as follows:

$$E(x,y,z,t) = E(x,y)e^{i(wt-\beta z)} \qquad (2.8)$$

where w and β are the angular frequency and propagation constant in z direction and are given by

$$w = \frac{2\pi v}{\lambda}, \qquad (2.9)$$

$$\beta = \frac{2\pi}{\lambda}.$$

(2.10)

Time-harmonics solution of the Maxwell equations is called the optical mode. Effective refractive index (n_{eff}) and group index (n_g) are the two fundamental characteristics of an optical mode.

2.2.1.1. Effective Index

The effective index provides a representation of the effective refractive index that a guided mode encounters. The effective index is calculated by solving the Maxwell's equations for the specific waveguide geometry and boundary conditions (Dattner & Yadid-Pecht, 2011).

2.2.1.2 Group Index

Although the effective index defines the speed that the phase of an optical wave propagates within a waveguide structure, it is insufficient to characterize the velocity of light in the waveguide, which is determined by the group velocity (Khare, 2004). The group index which is given Equation 2.11 is related to the speed light travels through the waveguide. It is derived from the relationship between the effective index, because of the dispersive characteristics of the waveguide.

$$n_g\,(\lambda) = \ n_{eff}\,(\lambda) - \left(\frac{dn_{eff}}{d_\lambda}\right)$$

(2.11)

$$v_g\left(\lambda\right) = \frac{c}{n_g}$$

As a result, the effective index by itself does not offer a comprehensive explanation of waveguide propagation behavior; it links to the group index, which determines the speed of light within the waveguide (Chrostowski & Hochberg, 2019).

2.2.2. Waveguide Geometry
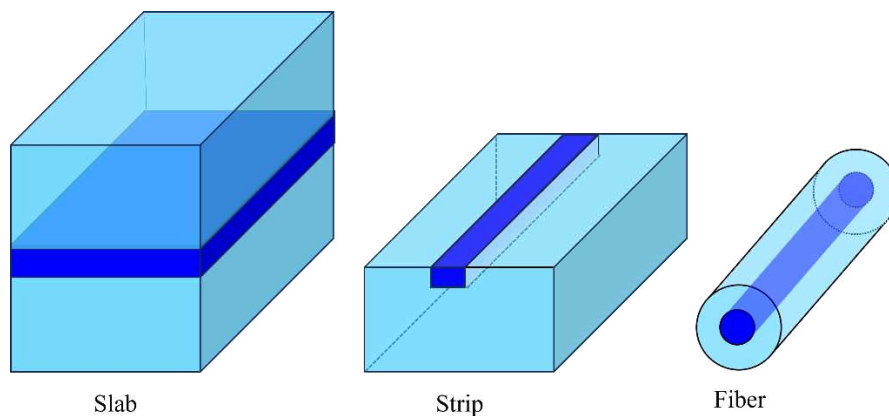
Figure 6. Optical waveguides (Source: (Saleh & Teich, 2018))

An optical waveguide is formed when a media with a high refractive index is embedded in or placed on a media with a lower refractive index. The geometry of an optical waveguide refers to its physical shape and dimensions. The shape of higher index media in which light is confined can be slab, strip and cylindrical can be seen Figure 6. Strip waveguides, which are widely used in photonic integrated circuits, have two common types: rib waveguides and ridge waveguides, as shown in Figure 7.
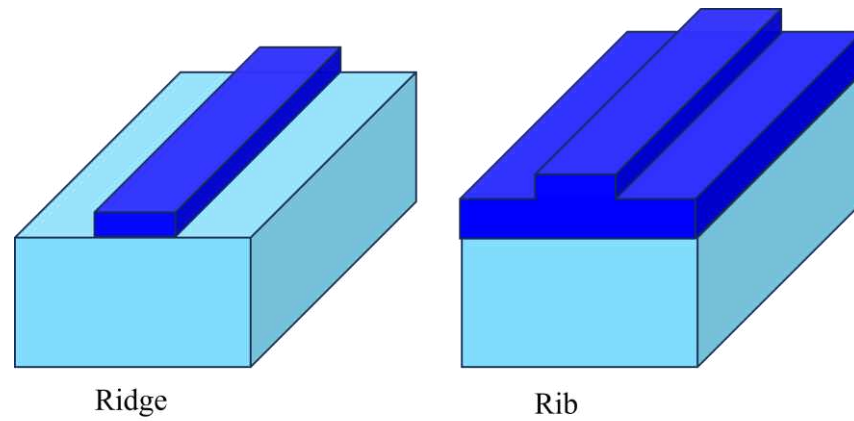
Figure 7. Ridge and rib type waveguides (Source: (Saleh & Teich, 2018))

The modes that can be supported in the waveguide can be tuned by adjusting the geometry of the optical waveguide. These modes can be calculated numerically, and they can also be found by conducting Finite-Difference Time-Domain (FDTD) analysis.

Through the application of the FDTD analysis method, a comprehensive examination of the mode confined within the waveguide in a two-dimensional context becomes possible. This analysis enables the determination of mode profiles for the quasi-TE and quasi-TM modes and facilitates the observation of crucial parameters such as electric field intensity, magnetic field intensity, and energy density. In particular, the analysis results pertaining to the electric field intensity, magnetic field intensity, and energy density of the 220x500 nm waveguide are illustrated in Figures 8, 9, and 10, respectively, at a wavelength of 1550 nm.

Figure 8 shows the fundamental mode profile, which is TE-like. The effective refractive index for this mode is 2.443. Although the field and energy are strongly coupled within the waveguide, approximately 10% of the field still resides in the cladding region. The effective index of TM-like mode which represents Figure 9 is 1.771 and the effective index encountered by the TE mode, which is the last mode supported, is 1.493, and the mode profile is shown in Figure 10.
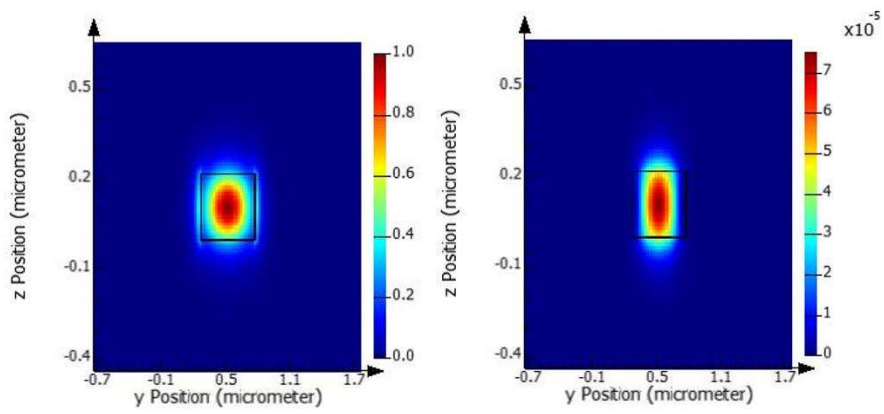
Figure 8. Mode profile belongs to the TE (first) mode (Source: (Chrostowski & Hochberg, 2019))
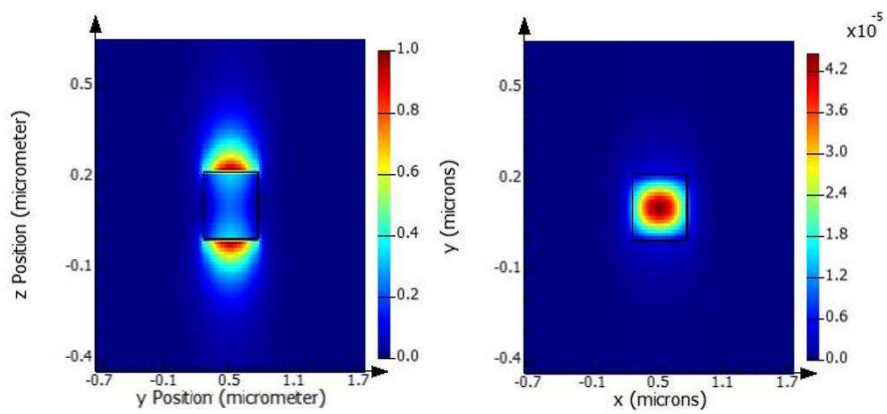
Figure 9. Mode profile belongs to the TM (second) mode (Source: (Chrostowski & Hochberg, 2019))

17
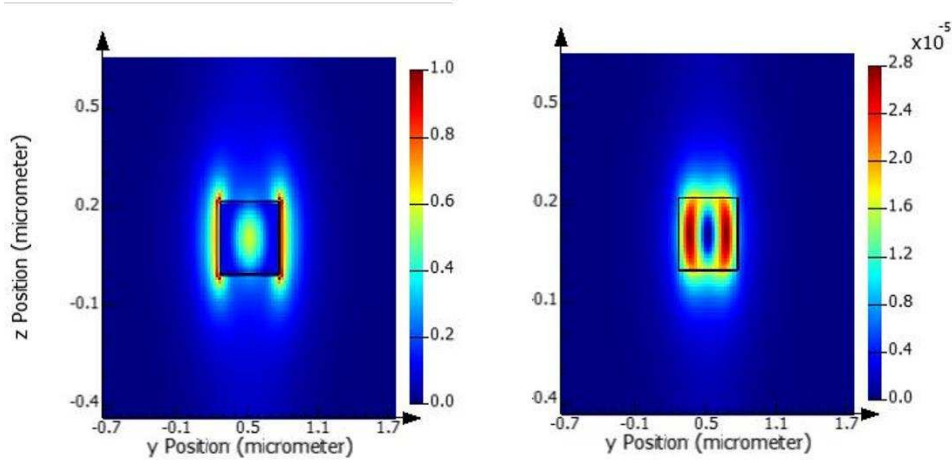
Figure 10. Mode profile of the TE (third) mode (Source: (Chrostowski & Hochberg, 2019))

2.3. Directional Couplers

Directional couplers are devices that allow the effective transmission of optical power from one waveguide to another allowing for the combination or splitting of light. The transition rate and the coupling coefficient are determined by the length of the couplers and the distance between the waveguides.

Coupled mode theory can be employed to determine the characteristics of a directional coupler (Yariv, 1973; Yariv 2006). The proportion of power which is transferred from one waveguide to another can be expressed as following equation:

$$K^2 = \frac{P_{cross}}{P_0} = sin^2 (C.L), \qquad (2.13)$$
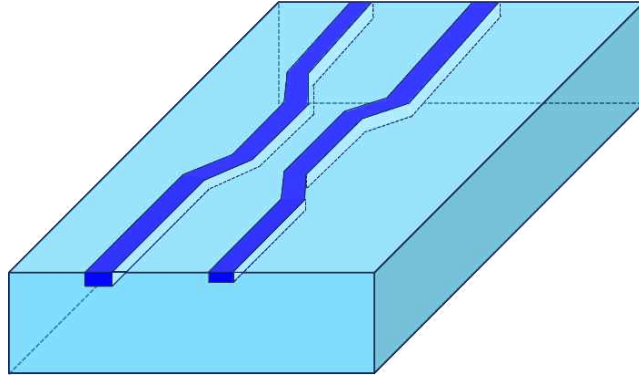
Figure 11. Schematic diagram of directional coupler (Source: (Saleh & Teich, 2018))

where P_{cross} is optical power transition between couplers and P_0 is the input optical power. C is coupling coefficient and L is the length of the coupler.

The ratio of the power that does not transferred to other couplers is

$$t^2 = \frac{P_{through}}{P_0} = cos^2 (C.L).$$ (2.14)

If it is assumed that coupling is lossless, the following equation can be written.

$$K^2 + t^2 = 1$$ (2.15)

2.4. Grating Couplers

Light coupling between optical fiber and waveguide is a challenge. The challenge lies in the significant difference in the dimensions of the fiber tip and the waveguide. Whereas the core diameter of the optical fiber typically ranges from 8 to 10 micrometers, the silicon waveguide's dimensions are on the order of several hundred nanometers.

Therefore, there are various fiber-to-chip coupling methods under two main categories: "edge coupling" and "surface coupling".
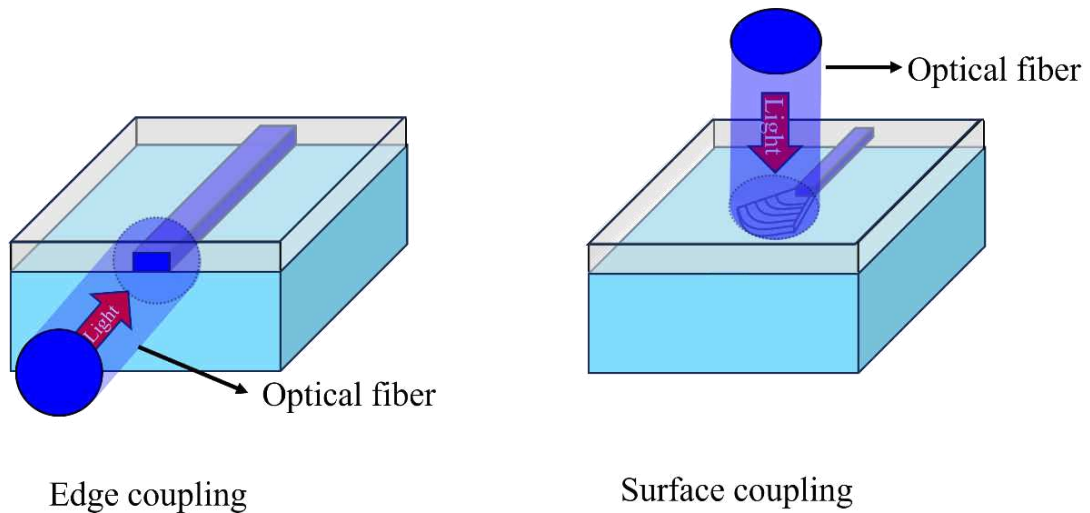
Figure 12. Edge coupling and surface coupling schematic

In the edge coupling, optical fiber is aligned horizontally with the waveguide from the wafer facet, as seen on the left of Figure 12. This method presents several notable advantages, including its ability to ensure a wide optical bandwidth and simultaneous support for both TE/TM modes, along with its alignment with established edge packaging techniques used for lasers and modulators. However, it is accompanied by certain disadvantages. These drawbacks include the requirement for the silicon chip to be positioned exclusively at the corners, resulting in a larger chip footprint and necessitating a complex fabrication process. This process entails tasks such as edge facet polishing, the implementation of tapers for mode expansion, and access to the chip's edge, further adding to its complexity (Mu et al., 2020).

An alternative approach is the utilization of grating couplers. Grating couplers are fabricated through etching or deposition that create refractive index variation on the chip surface. Thus, the projected light on the coupler surface as seen on the right of Figure 12 experiences Bragg diffraction by which some light is guided into the waveguide. This method exhibits several distinct advantages, including the ease of optical alignment, the ability to be integrated alongside waveguides without necessitating additional fabrication steps, and the flexibility to be placed anywhere on the chip as desired. These attributes collectively contribute to the favorable appeal of grating couplers as a coupling method.

Despite their numerous advantages, grating couplers also have disadvantages, notably the limitation of optical bandwidth and lower coupling efficiency. These limitations are important considerations when evaluating the applicability of grating couplers in optical systems and are tried to be overcome by numerous design techniques (Cheng et al., 2020).
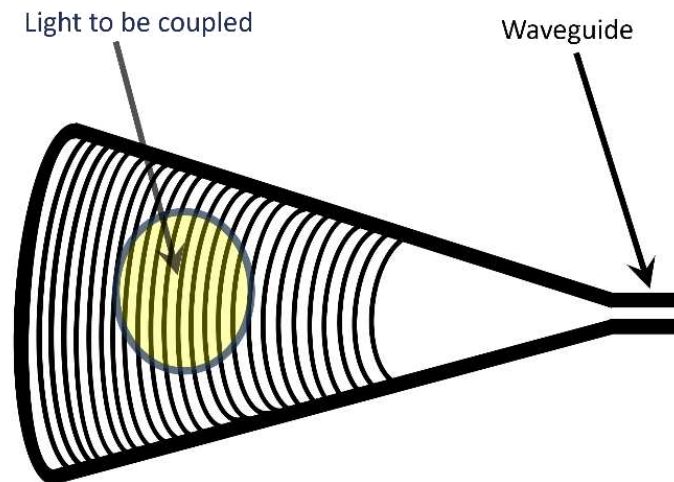
Figure 13. Grating coupling schematic (Source: (Chrostowski & Hochberg, 2019))

Figure 13 illustrates a grating coupler. The grating coupler is a periodic structure meticulously engineered to diffract light, which propagates from free space in an out-of-plane direction, into the waveguide residing within the plane of a silicon wafer. This particular coupler is tailored for TE polarization at a wavelength of 1550 nanometers, boasting a grating period of approximately 660 nanometers and the length of the coupler is about 30 microns. The output waveguide is situated on the right-hand side of the coupler for TE polarization.

2.5. Ring Resonator

2.5.1. Optical Transfer Function

The ring resonator shown in Figures 14 and 15 is assumed to be passive, with a lossless coupling. The analysis considers only single polarization, and there is no coupling of waves with different polarizations in any of the waveguide segments or coupler elements.
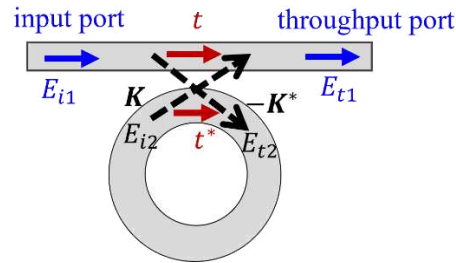
Figure 14. Single ring resonator with a directional coupler (Source: (Rabus, 2007))

Figure 14 shows a ring resonator with a directional coupler and gives notation used. Self-coupling coefficients and cross coupling coefficients are represented by t and t^* and K and K^*, respectively. The loss coefficient in ring resonator is denoted by α.

The roundtrip length is

$$L_{rt} = 2\pi r + 2L_c .\qquad(2.16)$$

where L_C is the coupler length. When ring resonator is point coupled, L_C equals to zero.

The relationship between the ring resonator and the waveguide is presented in the matrix below.

$$\begin{pmatrix} E_{t1} \\ E_{t2} \end{pmatrix} = \begin{pmatrix} t & K \\ -K^* & t^* \end{pmatrix} \begin{pmatrix} E_{i1} \\ E_{i2} \end{pmatrix} \tag{2.17}$$

The relationship between the electric fields in the ring resonator, considering it as a lossy structure, can be expressed as follows:

$$E_{i2} = e^{-i\phi_{rt}}\sqrt{e^{-\alpha L_{rt}}}\, E_{t2} \tag{2.18}$$

where α and ϕ_{rt} are attenuation constant and is round-trip optical phase and are given by

$$\phi_{rt} = \beta L_{rt}\,. \tag{2.19}$$

Since it is assumed that all optical loss is realized in the ring resonator, the following relation can be written between the coupling coefficients.

$$|\,K^2 + t^2\,| = 1 \tag{2.20}$$

Optical transfer function of all-pass ring resonator is

$$\frac{E_{t1}}{E_{in}} = \frac{-\sqrt{e^{-\alpha L_{rt}}} + te^{-i\phi_{rt}}}{-\sqrt{e^{-\alpha L_{rt}}}\, t^* + e^{-i\phi_{rt}}}\,. \tag{2.21}$$
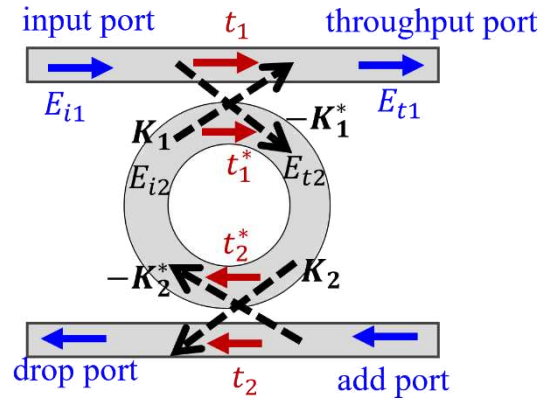
Figure 15. Add-drop type ring resonator (Source: (Rabus, 2007))

The optical transfer functions of add-drop type ring resonator are given by

$$\frac{E_{thr}}{E_{in}} = \frac{t_1 - {t_2}^* \sqrt{e^{-\alpha L_{rt}}}\; e^{i\phi_{rt}}}{1 - {t_1}^* {t_2}^* \sqrt{e^{-\alpha L_{rt}}}\; e^{i\phi_{rt}}}, \tag{2.22}$$

$$\frac{E_{thr}}{E_{in}} = \frac{-{K_1}^* K_2 \sqrt[4]{e^{-\alpha L_{rt}}}\; e^{i\phi_{rt/2}}}{1 - {t_1}^* {t_2}^* \sqrt{e^{-\alpha L_{rt}}}\; e^{i\phi_{rt}}} \tag{2.23}$$

where $e^{i\phi_{rt/2}}$ is the half round trip optical phase (Rabus, 2007).

2.5.2. Resonator Parameters Ring

The distance between two consecutive resonant wavelengths is called free spectral range (FSR) and it is calculated by the following formula.

$$FSR = \frac{\lambda^2}{n_g L_{rt}}$$

$$(2.24)$$

The resonance width is quantified by either the Full Width at Half Maximum (FWHM) or the 3 dB bandwidth of the resonance line shape, can be calculated as

$$FWHM = \frac{K^2 \lambda^2}{\pi\, n_{eff}\, L_{rt}}.$$

$$(2.25)$$

The Finesse (F) parameter of the ring resonator filter is defined as the ratio of the free spectral range and the width of a resonance for a specific wavelength. It is related to the level of narrowness exhibited by the resonances.

$$F = \frac{FSR}{FWHM}$$

$$(2.26)$$

The quality factor (Q) of a resonator is an indicator of the sharpness and effectiveness of its resonance, closely associated with the finesse parameter. It is an inherent parameter that cannot be directly measured but serves as a descriptive measure of the resonator's performance (Rabus, 2007).

$$Q = \frac{n_{eff}\ L_{rt}}{\lambda}\ F \qquad\qquad (2.27)$$

2.5.3. Temperature Dependency of Ring Resonators

As mentioned previously in section 2.1.1.2 Thermo-optic Effect in Silicon the effective refractive index of silicon varies with temperature. Since the optical properties of a ring resonator depend on the effective refractive index of the waveguide material, any temperature-induced changes in the refractive index will affect the performance of the resonator. Therefore, ring resonator structures are quite sensitive to temperature variations.

The temperature-dependent variation in the resonance wavelength of microring resonator is determined by

$$\frac{d\lambda_0}{dT} = \left(\frac{1}{L}\frac{\partial S}{dT}\right)\frac{\lambda_0}{n_g}, \qquad\qquad (2.28)$$

where L is the path length and S is the optical path length which can be calculated by multiplication of L and n_{eff}.

When the normalized temperature dependence equation is rearranged, the following equation is obtained by

$$\frac{1}{L}\frac{\partial S}{dT} = \left(n_{eff}\alpha_{sub} + \frac{\partial n_{eff}}{dT}\right), \qquad\qquad (2.29)$$

where λ_0 is resonance wavelength and α_{sub} is the thermal expansion coefficient of substrate. Although in some studies (Kokubun, Yoneda, & Tanaka, 1996) the effective index has been used instead of the group index in Equation 2.29, experimental studies have shown that using the group index yields more consistent results (Lee et al., 2008). This observation suggests that the group index is more suitable for characterizing the propagation behavior in certain situations. Therefore, it was preferable to use the group index instead of the effective refractive index.

The term thermal expansion coefficient mentioned is included in equation 2.29, focusing on the substrate, due to the significant difference in thickness between the waveguide and the substrate (Kokubun et al., 1993).

Due to the thermal expansion coefficient magnitude being on the order of 10^{-6} the thermal expansion coefficient can be neglected (Teng et al., 2009), and the equation for normalized temperature dependence can be rearranged as follows:

$$\frac{1}{L}\frac{dS}{dT} = \left(\frac{\partial n_{eff}}{dT}\right).$$

(2.30)

When equation 2.30 is substituted into equation 2.28, the equation for the temperature-dependent variation in the resonance wavelength becomes as follows:

$$\frac{d\lambda_0}{dT} = \left(\frac{\partial n_{eff}}{dT}\right)\frac{\lambda_0}{n_g}.$$

(2.31)

CHAPTER 3

METHODOLOGY

The aim of this thesis is to investigate the effect of temperature variation on the operation of a ring resonator. Firstly, a mathematical model has been developed, followed by simulating the required data for the mathematical model. Subsequently, designed devices have been fabricated and measured data compared with the numerical model.

3.1. Numerical Model

The numerical model is designed using MATLAB. The optical transfer functions of the ring resonator from the Background Information Chapter were utilized to simulate resonance wavelengths.

The optical transfer functions for the all-pass resonators are given by Equation 3.1.

$$\frac{E_{thr}}{E_{in}} = \frac{-\sqrt{e^{-\alpha L_{rt}}} + t e^{-i\phi_{rt}}}{-\sqrt{e^{-\alpha L_{rt}}} \, t^* + \, e^{-i\phi_{rt}}} \tag{3.1}$$

Equation 3.2 and Equation 3.3 are the transfer functions of the through and drop port of the add-drop type ring resonator, respectively.

$$\frac{E_{thr}}{E_{in}} = \frac{t_1 - t_2{}^*\sqrt{e^{-\alpha L_{rt}}} \, e^{i\phi_{rt}}}{1 - t_1{}^*t_2{}^*\sqrt{e^{-\alpha L_{rt}}} \, e^{i\phi_{rt}}} \tag{3.2}$$

$$\frac{E_{drop}}{E_{in}} = \frac{-K_1{}^*K_2\sqrt[4]{e^{-\alpha L_{rt}}}\,e^{i\phi_{rt/2}}}{1 - t_1{}^*t_2{}^*\sqrt{e^{-\alpha L_{rt}}}\,e^{i\phi_{rt}}} \tag{3.3}$$

The round-trip optical phase mentioned in this equation can be explained as described in the following equation:

$$\phi_{rt} = \beta L_{rt} = \frac{2\pi}{\lambda}\,n_{eff}L_{rt}\ . \tag{3.4}$$

Equation 3.4 refers to the effective index, which exhibits sensitivity to changes in both temperature and wavelength. To simulate the variation of refractive index with respect to temperature and wavelength, Lumerical MODE can be employed.

First of all, the variation of the refractive index with respect to the wavelength is assumed to be linear. By performing simulations at two different wavelengths, the variation of the refractive index according to the wavelength can be modeled as Equation 3.5.

$$n_{eff}(\lambda) = \ n_{eff,\lambda 2} + \frac{n_{eff,\lambda 1} - n_{eff,\lambda 2}}{\lambda_1 - \lambda_2}(\lambda - \lambda_2) \tag{3.5}$$

Since measurements are taken at two different temperatures, simulations for both temperatures must be done separately.

In the Lumerical MODE material database, there are silicon and silicon dioxide materials prepared according to Palik's handbook (Palik, 1998). Since measurements were conducted at 300 K, the materials in the database are not directly sensitive to temperature. Therefore, it is necessary to add a new material based on silicon to the database. A new material is created in the database and matched with silicon (Palik). Then, a value of 0.000187 (Frey & Leviton, 2006) is assigned as refractive index change per temperature value, and a reference temperature of 300 K is set. This way, a mathematically modeled temperature-sensitive silicon is created in the database.

The simulations were performed at wavelengths of 1550 nm and 1500 nm, and temperatures of 25 degrees and 35 degrees Celsius.

The simulation results performed at 398.1 K are presented in Figure 16.
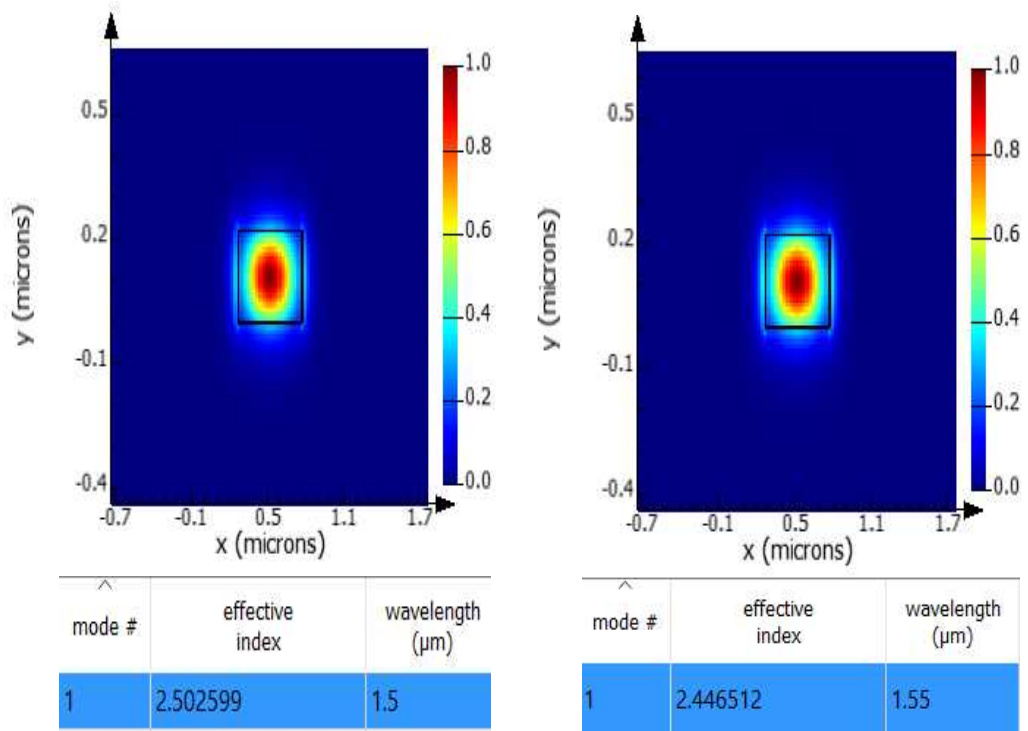

Figure 16. Simulated 220x500 nm waveguide at 1500 (left) and 1550 (right) nm at 298.1 K

The equation for the change in effective index depending on the wavelength at 25 degrees can be expressed as follows:

$$n_{eff}(\lambda) = \ 2.446512 - 1.12174(\lambda - 1550). \tag{3.6}$$

The results obtained from the simulations conducted at a temperature of 398.1 K are illustrated in Figure 17.
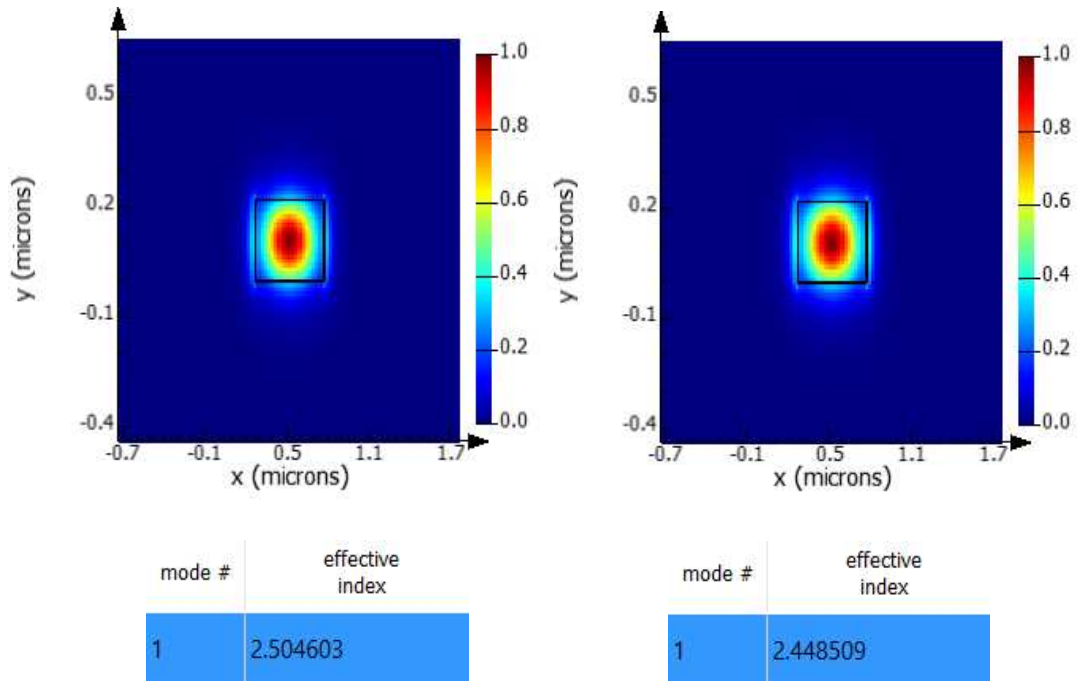
Figure 17. Simulated 220x500 nm waveguide at 1500 nm on left side and at 1550 nm on right side at 308.1 K

The following equation describes the relationship between the change in effective index and wavelength at a temperature of 35 degrees Celsius.

$$n_{eff}(\lambda) = \quad 2.4485509 - 1.12188(\lambda - 1550) \tag{3.7}$$

The simulations were conducted basically utilizing Equation 3.1 or Equations 3.2 and 3.3, depending on the resonator type, while considering temperature dependence through the use of Equation 3.6 and Equation 3.7.

3.2. Device Fabrication & Measurement

3.2.1. Device Fabrication

The fabrication of the devices was carried out using the NanoSOI MPW fabrication process, conducted by Applied Nanotools Inc. in Edmonton, Canada. The NanoSOI MPW fabrication method relies on direct-write 100 keV electron beam lithography as its primary technique. (Nanosoi Fabrication Service: Applied Nanotools Inc., 2020)

The photonic components were constructed on SOI wafers, characterized by a 200 mm diameter, a thickness of 220 nm, and a 2 µm buffer oxide layer. These wafers are initially partitioned into 25x25 mm squares, with the inclusion of scribe lines to simplify the division into smaller chips at a later stage.

The wafer was cleaned with water, IPA, and piranha solution (3:1 $H_2SO_4:H_2O_2$) for 15 minutes before being spin-coated with hydrogen silsesquioxane (HSQ) resist and heated to evaporate the solvent. The pattern of the components was achieved through the use of a Raith EBPG 5000+ electron beam tool with 5 nm precision step size. Following the construction of the pattern, an optical examination of the devices was conducted to identify any residues or anomalies.

Following the mounting of the chips onto a supporting wafer, they were exposed to an anisotropic ICP-RIE etching procedure with the utilization of chlorine. The resist was subsequently eliminated from the device surfaces through the use of a buffer oxide wet etching method, after which they underwent examination with the help of a scanning electron microscope.

In the final stage, the components were coated with a 2.2 µm oxide cladding layer through the application of a PECVD method. The device thicknesses were routinely validated during the process via reflectometry assessments.

3.2.2. Measurement

The measurements were carried out by Iman Taghavi at The University of British Columbia. Further details on the measurement process can be found in Chapter twelve of the book titled "Silicon Photonics Design: From Devices to Systems" authored by Lukas Chrostowski and Michael Hochberg (Chrostowski & Hochberg, 2015). In order to characterize the devices, a specially designed automated test setup (Maple Leaf Photonics, 2020) was utilized, equipped with automated control software written in Python developed by Michael Caverley. This setup enables precise and efficient execution of advanced experimental arrangements.

An Agilent 81600B tunable laser was employed as the input light source. This is a laser system that can operate over a wide wavelength range and provide a highly precise light output. For output detection, Agilent 81635A optical power sensors were used. These sensors can accurately measure the power of incoming light and ensure accurate data analysis.

During the experiments, the wavelength was swept from 1500 to 1600 nm. Each change was carried out in steps of 10 picometers (pm). This is essential for examining interactions of light at specific wavelengths.

A polarization maintaining fiber was used. This specialized fiber keeps the polarization state of the light constant, allowing for successful injection of TE polarization into the grating couplers (Wang et al., 2014). In order to couple light into and out of the device, a polarization-maintaining fiber array PLC Connections was used.

3.3. Examination Of Experimental and Theoretical Data

It is required to compare the measurement findings with the theoretical results in order to evaluate the performance of the fabricated ring resonators. Transferring the data of the measurement results to MATLAB and comparing them with the simulated data is an effective method for this purpose. In order to carry out this procedure, the experimental data should be converted to a similar format as the theoretical data through a variety of

processes. Another important issue is to analyze the data in the area where the effect of noise is as low as possible.
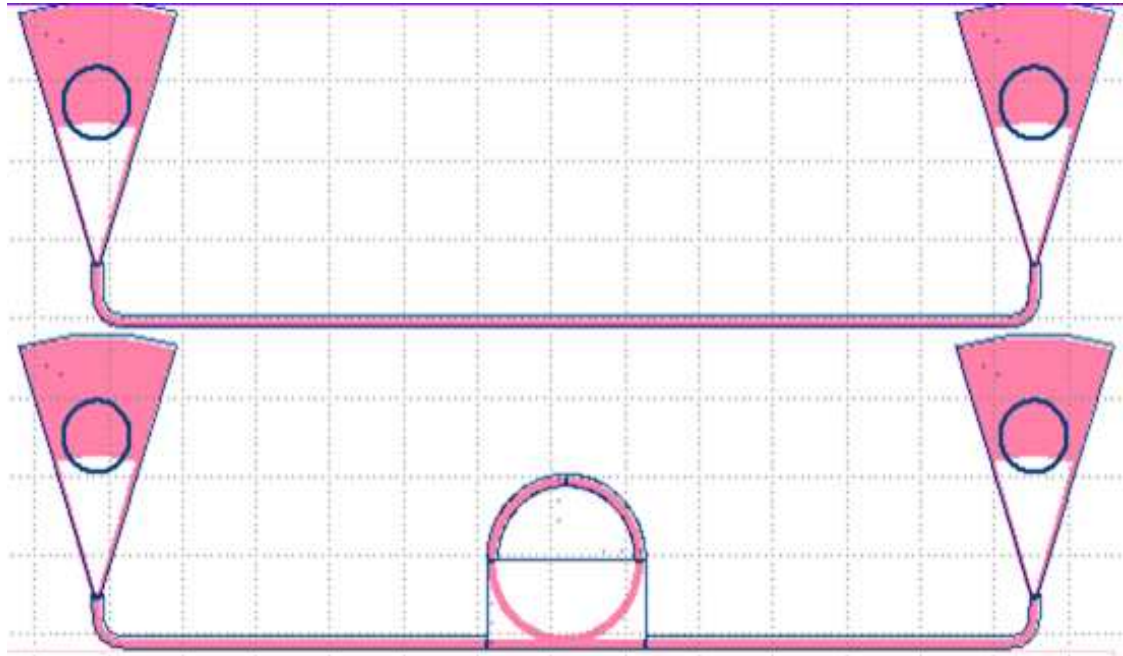

Figure 18. Calibration circuit(up) resonator circuit (down)

To diminish the possibility of confusion between the noise-related data and the resonator-related, one functional approach is to perform an analysis in the wavelength range that surpasses the highest 10 dB region in the spectrum. This can be achieved by creating a twin circuit using the ring resonator circuit depicted in Figure 18, where the resonator is removed from the circuit. Thus, effects except the resonator's influence can be observed in the spectrum.

Figure 19 shows a transmission graph of ring resonator circuit through port and Figure 20 between 1480 and 1580 nm of an example calibration circuit. In Figure 20 the blue line represents the transmission of the calibration circuit, and the red line drawn on it represents the highest 10 dB area.
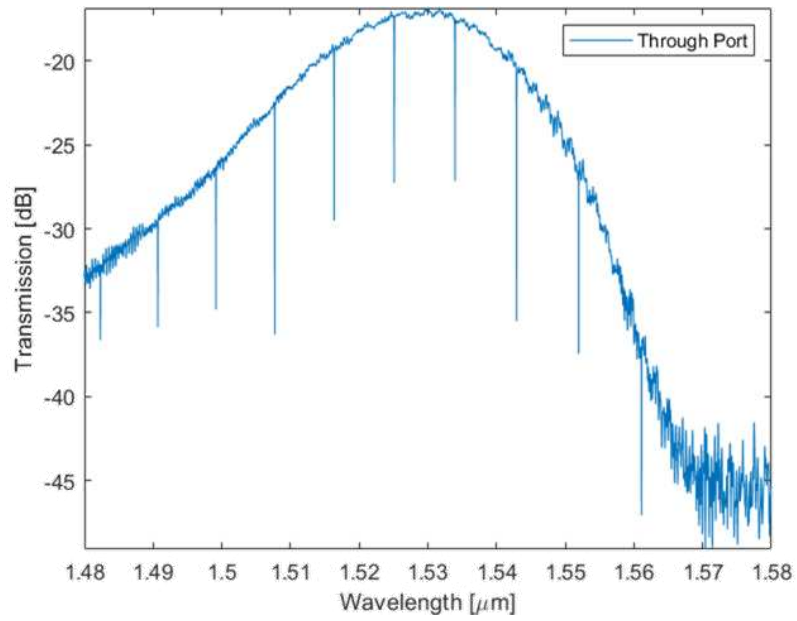
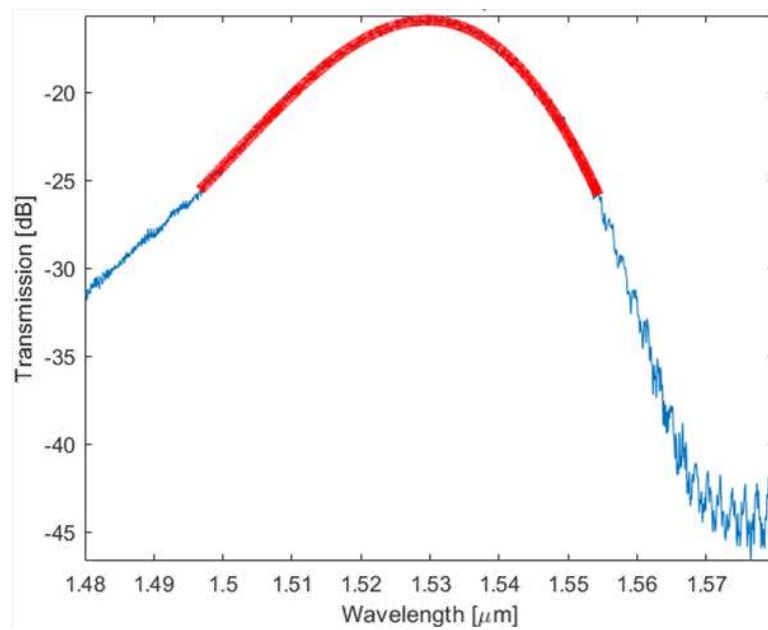Figure 19. Transmission spectrum of calibration circuit

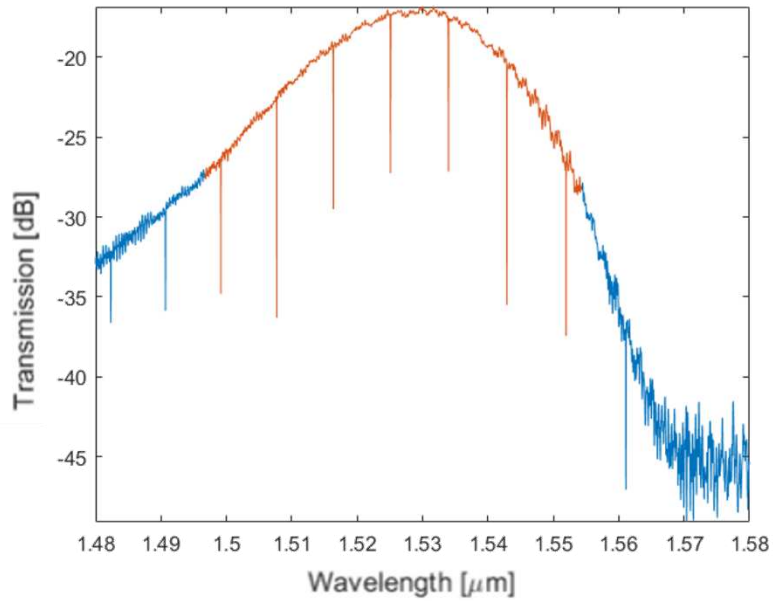Figure 20. Transmission spectrum of calibration circuit

Figure 21. Highest 10 dB area determined ring resonator transmission spectrum.

Once the wavelength range to be analyzed is determined, in order to flatten the elliptical transmission spectrum caused by the grating coupler, a peak point is identified in the spectrum. Separate low-order polynomial operations are then applied to the regions on the left and right of the peak to achieve a flatter transmission spectrum. This process results in a smoother transmission spectrum. Finally, the obtained values are normalized as can be seen in Figure 22.

Figure 23 displays the transmission spectrum of the ring resonator, which is generated based on a mathematical model. Similarly, the wavelength range corresponding to the best 10 dB region in the experimentally obtained spectrum is identified and normalized as can be seen Figure 24.
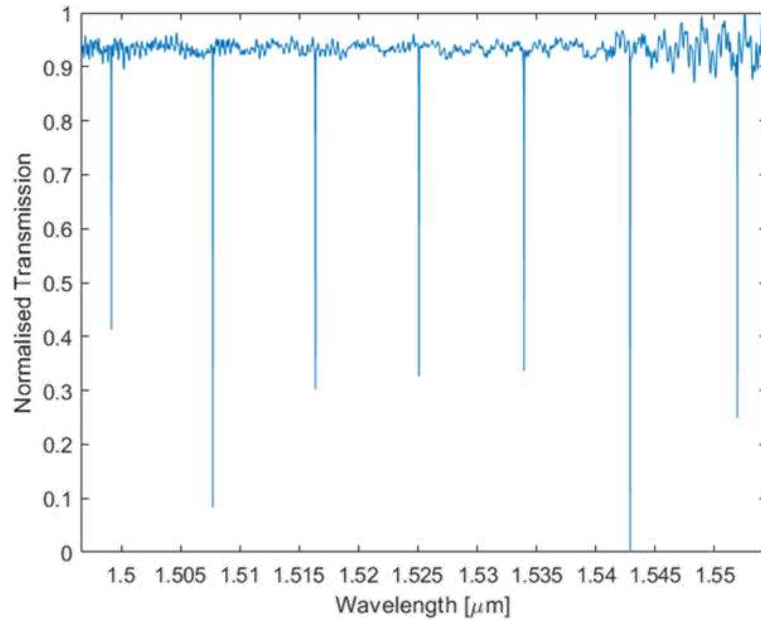
Figure 22. Normalized transmission spectrum of ring resonator
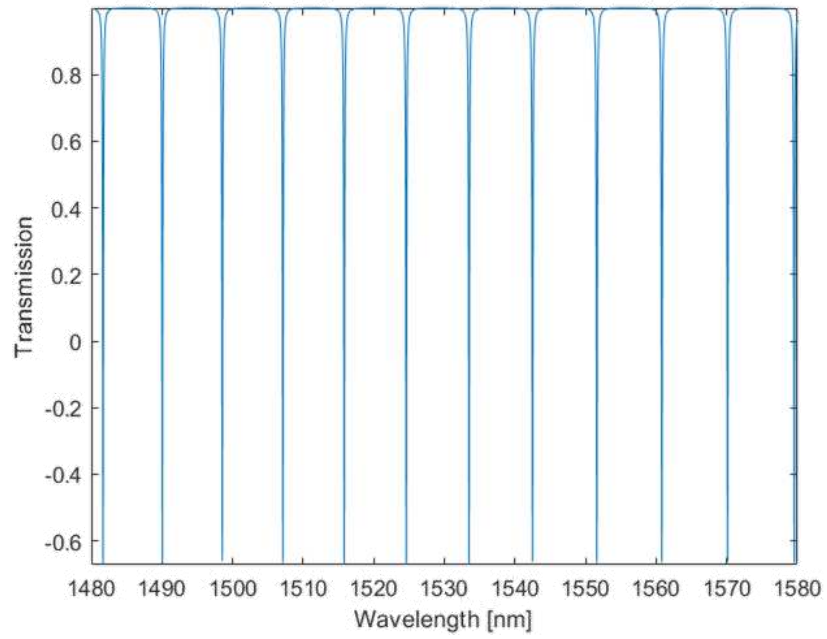
Figure 23. Theoretical transmission spectrum of ring resonator
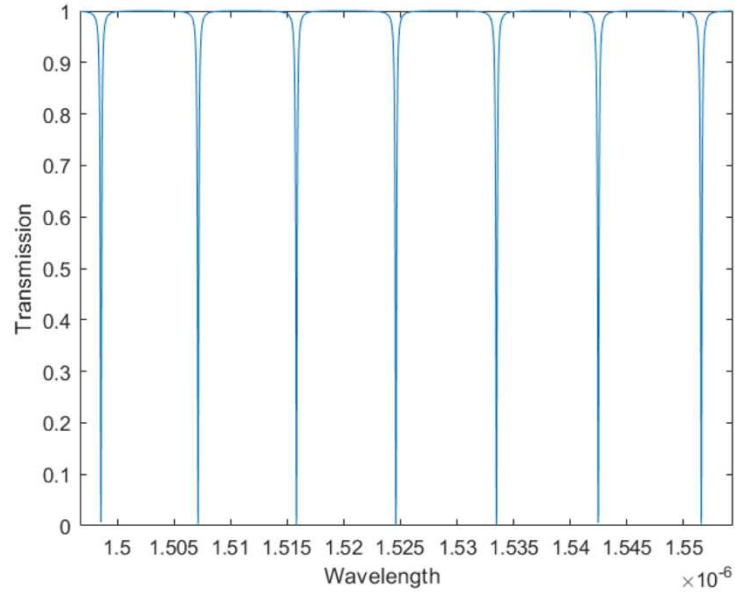
Figure 24. Normalized theoretical transmission spectrum of ring resonator

The error rate is determined by comparing the experimentally obtained resonance wavelengths, as indicated by the equation below, with the numerically calculated resonance wavelengths.

$$Error\ Rate\ (\%) = \frac{|Numerical\ \lambda_0 - Experimental\ \lambda_0|}{Numerical\ \lambda_0} \times 100 \qquad (3.8)$$

CHAPTER 4

RESULTS & DISCUSSION

In this section, two different types of resonators, namely all-pass and add-drop resonators, are examined. The focus is on investigating the relationship between numerical and experimental results and studying the variations in transfer functions with respect to temperature. The numerical simulations and experimental data are compared to gain insights into the feasibility of performance and behavior of resonators.

4.1. Results

4.1.1. Calibration Structure
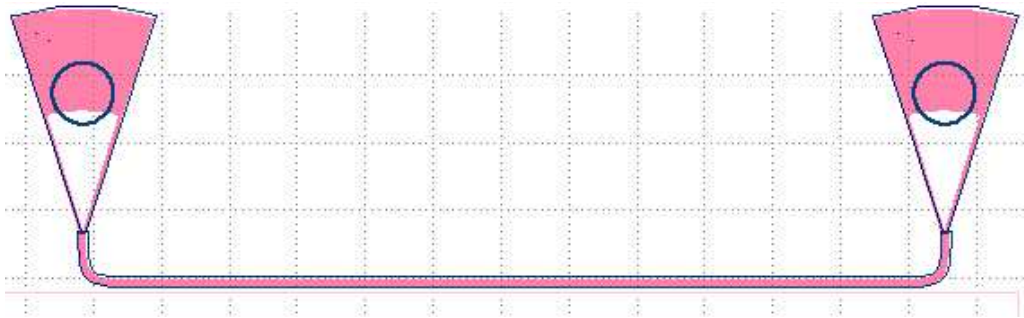
Figure 25. Calibration structure

In order to enhance the analysis of the experimental transmission spectrum, a measurement is also performed on a structure that lacks a resonator but possesses similar characteristics which was illustrated in Figure 25. Based on the experimental results, the top 10 dB region is identified, and this region is analyzed in structures with similar

characteristics due to the presence of grating couplers. This approach allows for the identification of the location with the least impact from noise.
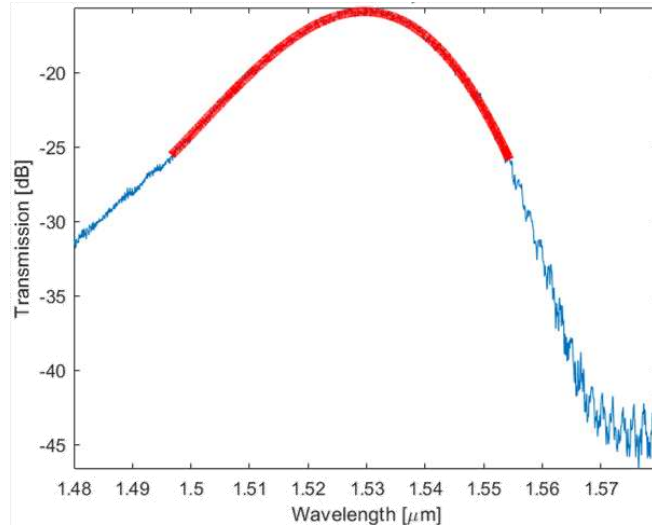
Figure 26. Transmission spectrum of calibration structure at 25 ˚C

The transmission spectrum of the calibration structure at 25 ˚C is in Figure 26. In Figure 20, the transmission of the calibration circuit is represented by the blue line, while the red line overlaid on it indicates the highest 10 dB region which will be to be determined as the analysis both 25 ˚C and 35 ˚C.

4.1.2. All-Pass Type Ring Resonator
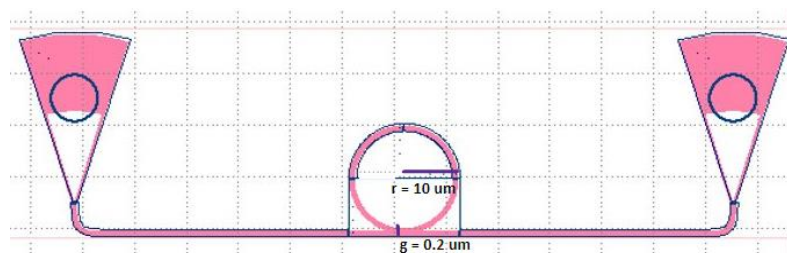
Figure 27. All-pass type ring resonator with radius of 10 μm and gap length of 0.2 μm

An all-pass type ring resonator with a radius of 10 micrometers, point-coupled, and a gap length of 0.2 micrometers has been investigated.
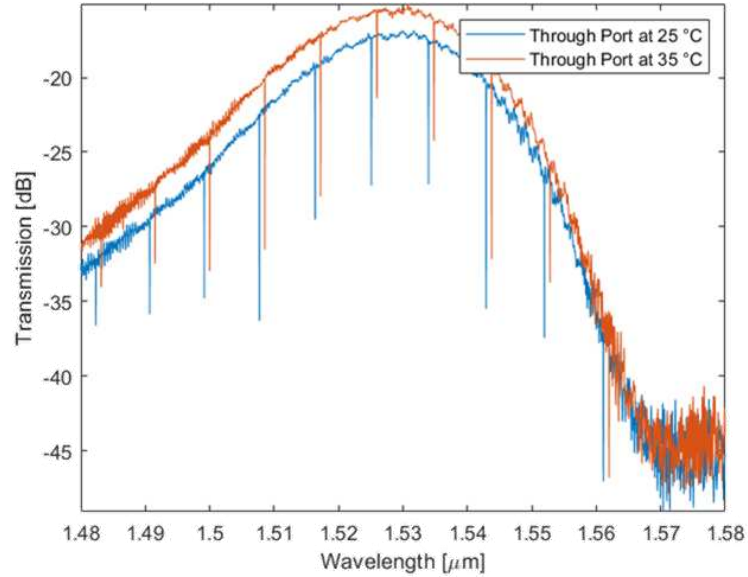
Figure 28. Experimental transmission spectrum of all-pass type ring resonator

The experimental transmission spectrum of the ring resonator is illustrated in Figure 28, in terms of dB. The calculated transmission spectrum is depicted in Figure 29. The blue lines represent the transmission spectrum at 25 degrees, while the red lines represent the transmission spectrum at 35 degrees. The elliptical shape of the spectrum is attributed to the presence of grating couplers, which facilitate the optical input and the output.
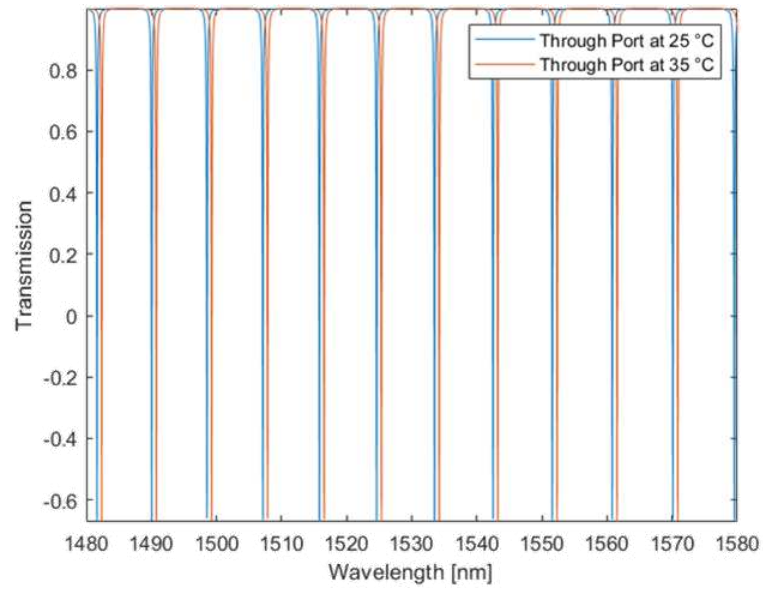
Figure 29. Theoretical spectrum of all-pass ring resonator
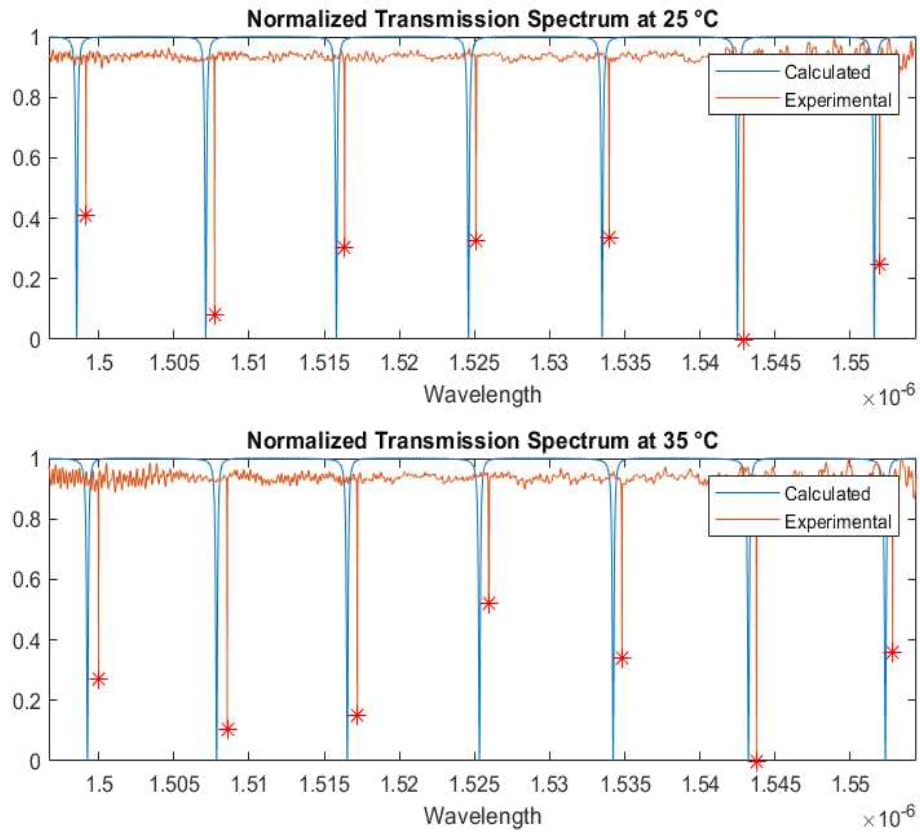
Figure 30. Normalized transmission spectrum of calculated and experimental results of ring resonator at 25 ˚C(up) at 35 ˚C(down)

The resonance wavelengths of the experimental and numerical results at 25 ˚C and 35 ˚C, as well as the error rates calculated, are given in the table below for the all-pass ring resonator structure with a radius of 10 micrometers. The resolution of the spectrum measurements was 10 picometers which is high enough to obtain 6 significant figures in the results, which allowed for more precise error calculation.

Table 1. Numerical and experimental resonance wavelength (μm) and their error rate

Numerical 25 ˚C	Experimental 25 ˚C	Error Rate 25 C˚ (%)	Numerical 35 ˚C	Experimental 35 ˚C	Error Rate 35 ˚C (%)
1.49854	1.49915	0.040706	1.49925	1.49999	0.049358
1.50712	1.50771	0.039148	1.50784	1.50855	0.047087
1.51581	1.51636	0.036284	1.51654	1.51720	0.04352
1.52460	1.52509	0.03214	1.52533	1.52594	0.039991
1.53349	1.53396	0.030649	1.53422	1.53481	0.038456
1.54249	1.54291	0.027229	1.54322	1.54376	0.034992
1.55159	1.55195	0.023202	1.55233	1.55281	0.030921

4.1.3. Add-Drop Type Ring Resonator
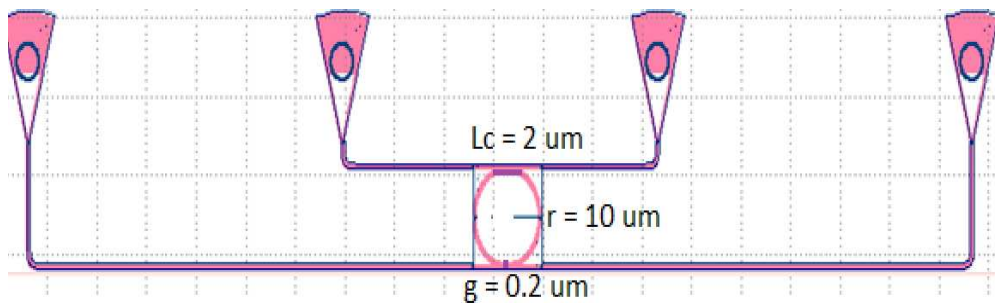
Figure 31. Add-drop type ring resonator with radius 10 μm, coupling length 2 μm and gap length is 0.2 μm

An investigation was conducted on a ring resonator of the add-drop type, featuring a radius of 10 micrometers, a coupling length 2 micrometers, and a gap length of 0.2 micrometers.
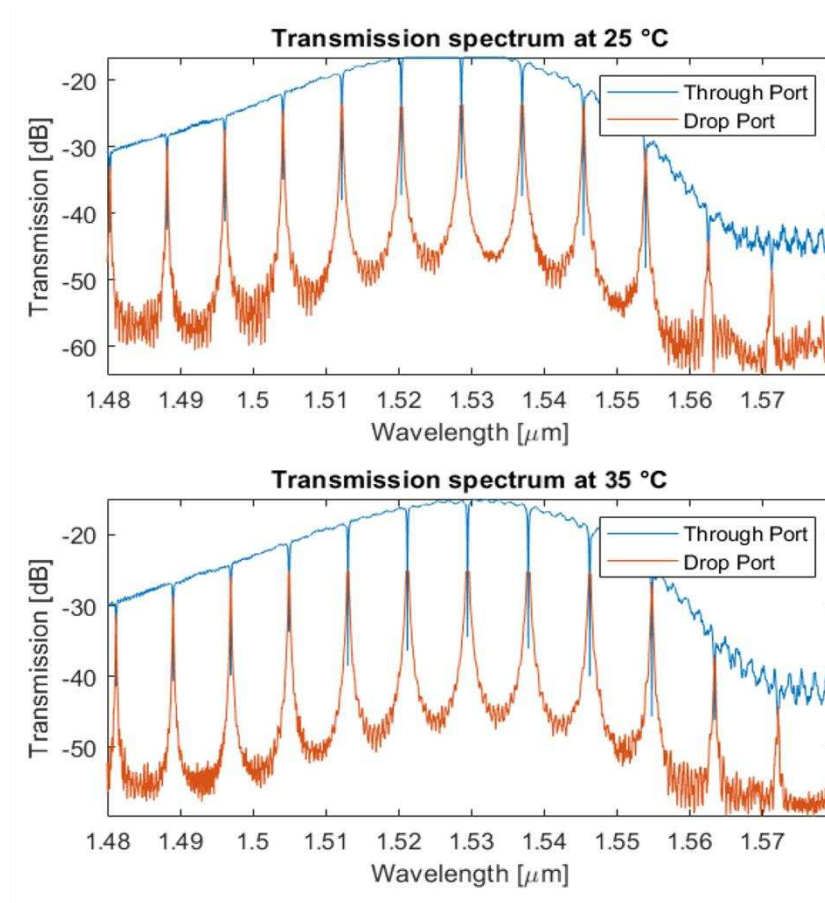
Figure 32. Add-drop type ring resonator experimental transmission spectrum at 25 ˚C (up) and 35 ˚C(down)

Experimental transmission spectrum of an add-drop ring resonator at 25 ˚C and 35 ˚C are shown in Figure 32. Red lines represent the output at the drop port, while blue lines represent the output at the through port.

The temperature-dependent shift of the transmission spectra at the drop port and the through ports are illustrated in Figure 33. The red lines belong to the 25 ˚C and the blue lines belong to the spectrum at 35 ˚C.

The normalized spectra data obtained through numerical analysis is depicted in Figure 34.
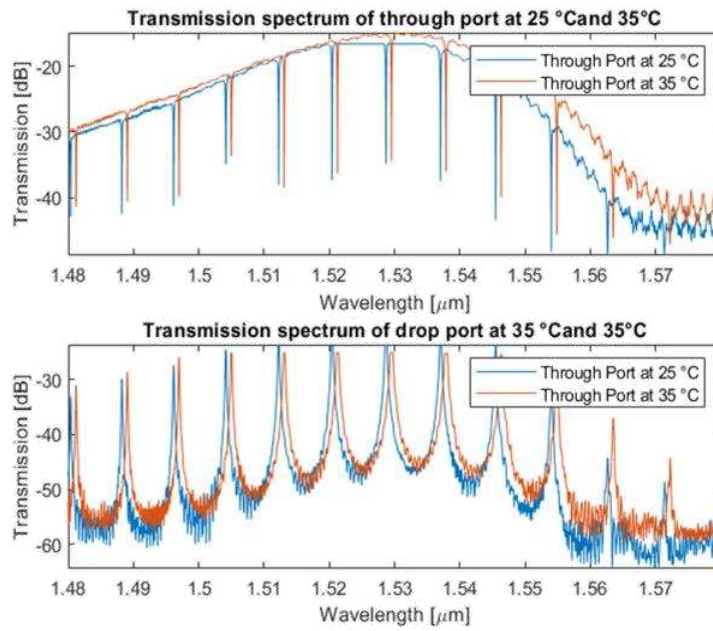
Figure 33. The experimental transmission graphs for the through (up) and drop (down) ports at 25 ˚C and 35 ˚C
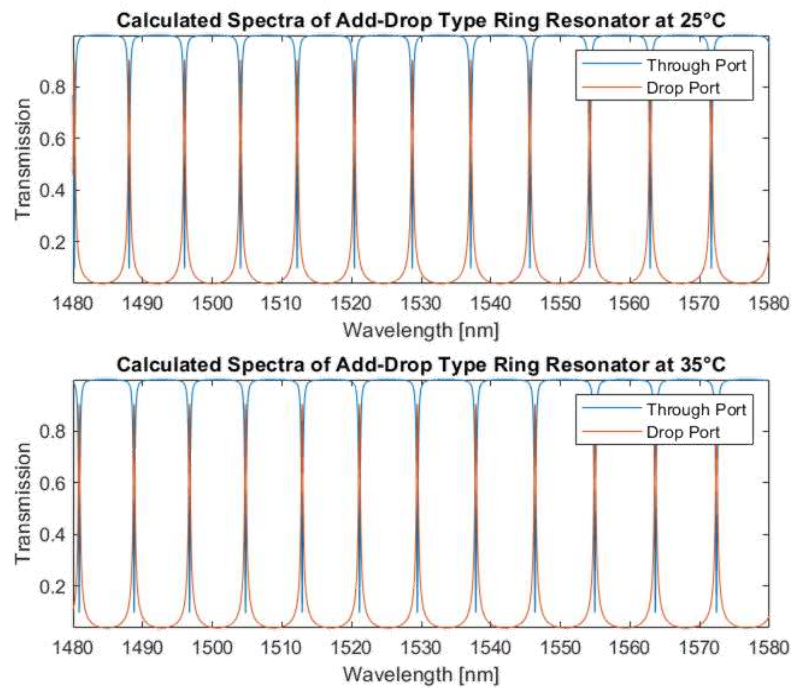
Figure 34. Numerically calculated transmission spectrum of add-drop ring resonator at 25 ˚C and 35 ˚C
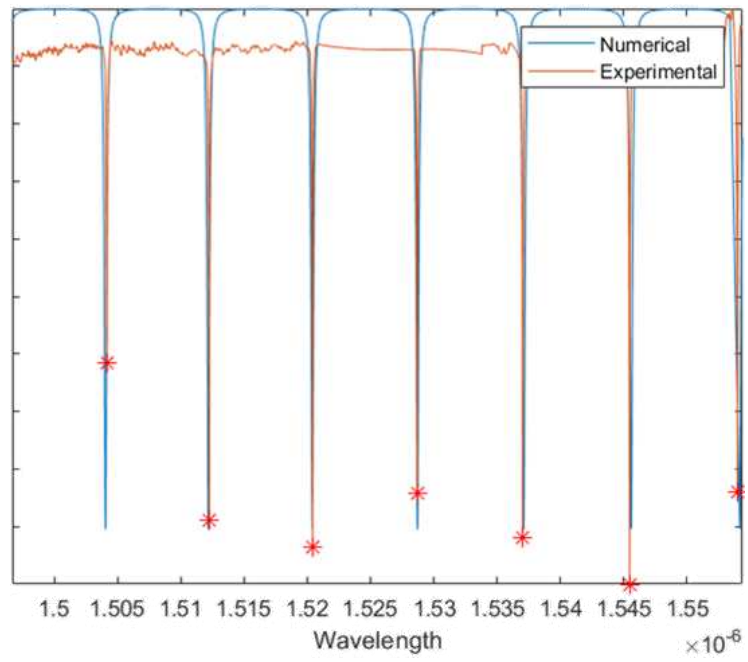
Figure 35. Normalized experimental and numerically calculated spectra belongs to through port at 25 ˚C
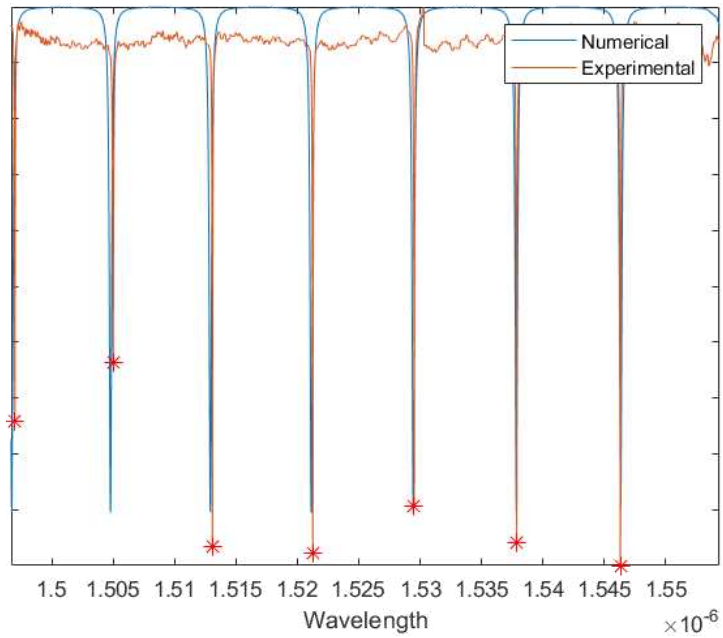
Figure 36. Normalized experimental and numerically calculated spectra belongs to through port at 35 C˚

The normalized and calibrated measured spectra and numerical data at 25 and 35 degrees Celsius, with a maximum of 10 dB as the reference point, are presented in Figures 34 and 35. The resonance frequencies and the corresponding error rates calculated based on the resonance wavelengths are provided in Table 2.

Table 2. Numerical and experimental resonance wavelength (μm) and their error rate

| Calculated λ_0 25 ˚C	Measured λ_0 25 ˚C	Error Rate 25 ˚C (%)	Calculated λ_0 35 ˚C	Measured λ_0 35 ˚C	Error Rate 35 ˚C (%)
1.50405	1.50415	0.006649	1.49672	1.49697	0.016703
1.51218	1.51224	0.003968	1.50477	1.50498	0.013956
1.50405	1.50415	0.006649	1.51291	1.51308	0.011237
1.52871	1.52868	0.001962	1.52113	1.52126	0.008546
1.53711	1.53703	0.005205	1.52944	1.52952	0.005231
1.54561	1.54548	0.008411	1.53785	1.53788	0.001951
1.55419	1.55401	0.011582	1.54634	1.54632	0.001293

4.2. Discussion

Ring resonators, designed as add-drop and all-pass types, have been numerically analyzed, fabricated, and measured. The data, which belongs to the experimental studies and numerical analyses conducted separately for 25 ˚C degrees and 35 ˚C has been successfully analyzed.

As confirmed by the experimental results, there exists a correlation between the increase in temperature and the shift of the resonance wavelength towards higher values. This result agrees with the theoretical expectations and underlines the validity of the model established for the study. The consistency of these findings, with an error range from approximately 0.00112% to 0.0049%, demonstrates the accuracy and reliability of the model and the experimental setup. These results help us to understand how temperature affects the properties of ring resonators.

CHAPTER 5

CONCLUSION

In conclusion, this study has successfully demonstrated that temperature variations do indeed impact the performance of ring resonators. Numerical model construction, fabrication, measurement, and data analyses have been conducted at 25 °C and 35 °C, yielding consistent results and reinforcing the robustness of the study. As temperature increases, a consistent shift towards higher resonance wavelengths was observed, which confirmed the objective of this thesis. The experimental results showed a clear correlation between the numerical model when temperature increase and resonance wavelength shift due to temperature increases, with an error rate ranging from 0.00112% to 0.0049%. Temperature changes significantly affect the performance of silicon photonic circuits, thus making the analysis of these systems at different temperatures a critical issue. On the other hand, ring resonator structures can also be used as temperature sensors. In this thesis, the impact of temperature on ring resonators, which are passive photonic circuit structures, has been examined. Although the error rate has been as well as 0.00112%, there is still much work to be done to broaden their use and expand their application areas. These future works can be primarily listed as follows.

- Conducting measurements in a wider temperature range consisting of more samples with smaller steps. Carrying out research to increase sensitivity to smaller temperature changes, primarily for temperature sensors.
- Conducting measurements with different waveguide geometries and resonators.
- Investigating athermal ring resonator structures resistant to temperature changes for self-referenced sensors.
- Setting up closely placed ring resonators or other silicon circuits to conduct cross-talk analysis with varying temperatures.
- Going beyond numerical analysis to conduct complex simulations.
- Fabricating and measuring large number of identical ring resonator structures to calculate the mean error and standard deviation.

REFERENCES

Alam, M. Z., Moreno, J., Aitchison, J. S., Mojahedi, M., & Kazemi, A. A. 2008. "Integrated Multi-Channel Nano-Engineered Optical Hydrogen and Temperature Sensor Detection Systems for Launch Vehicles." P. 70950O in *Nanophotonics and Macrophotonics for Space Environments II*. Vol. 7095. SPIE.

Biberman, A., Lira, H. L., Padmaraju, K., Ophir, N., Chan, J., Lipson, M., & Bergman, K. (2011). Broadband Silicon Photonic electrooptic switch for photonic interconnection networks. *IEEE Photonics Technology Letters*, *23*(8), 504–506. doi:10.1109/lpt.2011.2112763

Bogaerts, W., De Heyn, P., Van Vaerenbergh, T., De Vos, K., Kumar Selvaraja, S., Claes, T., Dumon, P., Bienstman, P., Thourhout, V., Baets, R. (2011). Silicon microring resonators. *Laser & Photonics Reviews*, *6*(1), 47–73. doi:10.1002/lpor.201100017

Bogaerts, Wim, Fiers, M., & Dumon, P. (2014). Design challenges in Silicon Photonics. *IEEE Journal of Selected Topics in Quantum Electronics*, *20*(4), 1–8. doi:10.1109/jstqe.2013.2295882

Bogaerts, W., & Selvaraja, S. K. (2014). Silicon-on-insulator (SOI) technology for photonic integrated circuits (PICS). Silicon-On-Insulator (SOI) Technology, 395–434. doi:10.1533/9780857099259.2.395

Burla, M., Cortés, L. R., Li, M., Wang, X., Chrostowski, L., & Azaña, J. (2013). Integrated Waveguide Bragg gratings for Microwave Photonics Signal Processing. *Optics Express*, *21*(21), 25120. doi:10.1364/oe.21.025120

Chen, L., & Lipson, M. (2009). Ultra-low capacitance and high speed germanium photodetectors on Silicon. *Optics Express*, *17*(10), 7901. doi:10.1364/oe.17.007901

Cheng, L., Mao, S., Li, Z., Han, Y., & Fu, H. Y. (2020). Grating Couplers on Silicon Photonics: Design Principles, Emerging Trends and Practical Issues. Micromachines, 11(7), 666. https://doi.org/10.3390/mi11070666

Chrostowski, L., & Hochberg, M. (2019). *Silicon Photonics Design*. Cambridge: Cambridge University Press.

Dattner, Y., & Yadid-Pecht, O. (2011). Analysis of the effective refractive index of silicon waveguides through the constructive and destructive interference in a mach–zehnder interferometer. IEEE Photonics Journal, 3(6), 1123–1132. doi:10.1109/jphot.2011.2171678

Debrégeas-Sillard, H., & Kazmierski, C. (2008). Challenges and advances of photonic integrated circuits. *Comptes Rendus Physique*, *9*(9–10), 1055–1066. doi:10.1016/j.crhy.2008.10.004

Doylend, J. K., Heck, M. J., Bovington, J. T., Peters, J. D., Coldren, L. A., & Bowers, J. E. (2011). Two-dimensional free-space beam steering with an optical phased array on silicon-on-insulator. *Optics Express*, *19*(22), 21595. doi:10.1364/oe.19.021595

Dumon, P. (2007) *Ultra-compact integrated optical filters in silicon-on-insulator by means of wafer-scale technology*. PhD Thesis. Gent University.

Foster, M. A., Turner, A. C., Lipson, M., & Gaeta, A. L. (2008). Nonlinear optics in photonic nanowires. *Optics Express*, *16*(2), 1300. doi:10.1364/oe.16.001300

Frey, B. J., Leviton, D. B., & Madison, T. J. (2006). Temperature-dependent refractive index of silicon and Germanium. *SPIE Proceedings*. doi:10.1117/12.672850

Geuzebroek, D. H., & Driessen, A. (2006). Ring-resonator-based wavelength filters. *Springer Series in Optical Sciences*, 341–379. doi:10.1007/3-540-31770-8_9

Hochberg, M., Harris, N. C., Ding, R., Zhang, Y., Novack, A., Xuan, Z., & Baehr-Jones, T. (2013). Silicon Photonics: The next fabless semiconductor industry. *IEEE Solid-State Circuits Magazine*, *5*(1), 48–58. doi:10.1109/mssc.2012.2232791

Hsu, W.-C., Nujhat, N., Kupp, B., Conley, J. F., & Wang, A. X. (2023). On-chip wavelength division multiplexing filters using extremely efficient gate-driven silicon microring resonator array. *Scientific Reports*, *13*(1). doi:10.1038/s41598-023-32313-0

Hu, J., Sun, X., Agarwal, A., & Kimerling, L. C. (2009). Design guidelines for optical resonator biochemical sensors. *Journal of the Optical Society of America B*, *26*(5), 1032. doi:10.1364/josab.26.001032

Khare, R. P. (2004). *Fiber optics and Optoelectronics*. New Delhi: Oxford University Press.

Kim, Gun-Duk, Hak-Soon Lee, Chang-Hyun Park, Sang-Shin Lee, Boo Tak Lim, Hee Kyoung Bae, & Wan-Gyu Lee. 2010. "Silicon Photonic Temperature Sensor Employing a Ring Resonator Manufactured Using a Standard CMOS Process." *Optics Express* 18(21):22215–21. doi: 10.1364/OE.18.022215.

Kim, Hyun-Tae, & Miao Yu. 2016. "Cascaded Ring Resonator-Based Temperature Sensor with Simultaneously Enhanced Sensitivity and Range." *Optics Express* 24(9):9501. doi: 10.1364/oe.24.009501.

Klimov, Nikolai, Michaela Berger, and Zeeshan Ahmed. 2015. "Towards Reproducible Ring Resonator Based Temperature Sensors." *Sensors & Transducers* 191(8):63–66.

Ko, M., Youn, J.-S., Lee, M.-J., Choi, K.-C., Rucker, H., & Choi, W.-Y. (2012). Silicon Photonics-wireless interface IC for 60-GHz wireless link. *IEEE Photonics Technology Letters*, *24*(13), 1112–1114. doi:10.1109/lpt.2012.2196034

Kokubun, Y., Funato, N. and Takizawa, M. (1993) 'Athermal waveguides for temperature-independent lightwave devices', *IEEE Photonics Technology Letters*, 5(11), pp. 1297–1300. doi:10.1109/68.250049.

Kokubun, Y., S. Yoneda, & H. Tanaka. 1996. "Temperature-Independent Narrowband Optical Filter at 1.3 µ m Wavelength by an Athermal Waveguide." *Electronics Letters* 32(21):1998–200.

Komljenovic, T., Liang, L., Chao, R.-L., Hulme, J., Srinivasan, S., Davenport, M., & E. Bowers, J. (2017). Widely-tunable ring-resonator semiconductor lasers. *Applied Sciences*, *7*(7), 732. doi:10.3390/app7070732

Lee, B. G., Small, B. A., Xu, Q., Lipson, M., & Bergman, K. (2007). Characterization of a 4×4 GB/S parallel electronic bus to WDM optical link silicon photonic translator. *IEEE Photonics Technology Letters*, *19*(7), 456–458. doi:10.1109/lpt.2007.893032

Lee, J.-M., Kim, D.-J., Kim, G.-H., Kwon, O.-K., Kim, K.-J., & Kim, G. (2008). Controlling temperature dependence of silicon waveguide using slot structure. Optics Express, 16(3), 1645. doi:10.1364/oe.16.001645

Li, G., Zheng, X., Yao, J., Thacker, H., Shubin, I., Luo, Y., Raj, K., John, E. C., & Krishnamoorthy, A. V. (2011). 25GB/s 1v-driving CMOS ring modulator with integrated thermal tuning. *Optics Express*, *19*(21), 20435. doi:10.1364/oe.19.020435

Liu, H., Wang, T., Jiang, Q., Hogg, R., Tutu, F., Pozzi, F., & Seeds, A. (2011). Long-wavelength Inas/GaAs quantum-dot laser diode monolithically grown on GE substrate. *Nature Photonics*, *5*(7), 416–419. doi:10.1038/nphoton.2011.120

Luo, Haiyan, Lu Xu, Jie Yan, Qiansheng Wang, Wenwu Wang, & Xi Xiao. 2023. "High-Resolution Silicon Photonic Sensor Based on a Narrowband Microwave Photonic Filter." *Frontiers of Optoelectronics* 16(1). doi: 10.1007/s12200-023-00059-2.

Maple Leaf Photonics (2020). Retrieved from http://mapleleafphotonics.com/

Mu, X., Wu, S., Cheng, L., & Fu, H. Y. (2019). Edge Couplers in Silicon Photonic Integrated Circuits: A Review. Applied Sciences, 10(4), 1538. doi: 10.3390/app10041538

Nanosoi Fabrication Service: Applied Nanotools Inc. (2020). Retrieved from http://www.appliednt.com/nanosoi

Palik, E. D. (1998). *Handbook of Optical Constants of Solids*. London: Academic Press.

Pathak, S. (2019). Photonics Integrated Circuits. *Nanoelectronics*, 219–270. doi:10.1016/b978-0-12-813353-8.00008-7

Pavesi, L. & Guillot G. (2006). *Optical Interconnects: The Silicon Approach.* Springer Berlin/Heidelberg.

PLC Connections. Retrieved from https://www.plcconnections.com/

Rabus, D. G. (2007). *Integrated Ring Resonators the Compendium*. Berlin: Springer.

Saleh, B. E. A., & Teich, M. C. (2018b). *Fundamentals of photonics*. New Delhi: Wiley.

Teng, J., Dumon, P., Bogaerts, W., Zhang, H., Jian, X., Han, X., Zhao, M., Morthier, G., & Baets, R. (2009). Athermal silicon-on-insulator ring resonators by overlaying a polymer cladding on narrowed waveguides. *Optics Express*, *17*(17), 14627. doi:10.1364/oe.17.014627

The lure of silicon. (2007). Nature Photonics 1(4), 187. doi: 10.1038/nphoton.2007.33

Thomson, David, Aaron Zilkie, John E. Bowers, Tin Komljenovic, Graham T. Reed, Laurent Vivien, Delphine Marris-Morini, Eric Cassan, Léopold Virot, Jean-Marc Fédéli, Jean-Michel Hartmann, Jens H. Schmid, Dan-Xia Xu, Frédéric Boeuf, Peter O'Brien, Goran Z. Mashanovich, & M. Nedeljkovic. 2016. "Roadmap on Silicon Photonics." *Journal of Optics* 18(7):073003. doi: 10.1088/2040-8978/18/7/073003.

Wang, Y., Wang, X., Flueckiger, J., Yun, H., Shi, W., Bojko, R., Nicolas, A., F., J., & Chrostowski, L. (2014). Focusing sub-wavelength grating couplers with low back reflections for rapid prototyping of silicon photonic circuits. *Optics Express*, *22*(17), 20652. doi:10.1364/oe.22.020652

Wang, Jin, Yijie Pan, Jianxin Gao, Cheng Zhang, Zhier Qu, Tongtong Xu, Yang Shen, & Jifeng Qu. 2022. "An On-Chip Silicon Photonics Thermometer with Milli-Kelvin Resolution." *Applied Sciences (Switzerland)* 12(8). doi: 10.3390/app12083713.

Xu, H., Hafezi, M., Fan, J., Taylor, J. M., Strouse, G. F., & Ahmed, Z. 2014. "Ultra-Sensitive Chip-Based Photonic Temperature Sensor Using Ring Resonator Structures." *Optics Express* 22(3):3098. doi: 10.1364/oe.22.003098.

Yariv, A. (1973). Coupled-mode theory for guided-wave optics. *IEEE Journal of Quantum Electronics*, *9*(9), 919–933. doi:10.1109/jqe.1973.1077767

Yariv, A. & Yeh, P. (2006) Photonics: Optical Electronics in Modern Communications. Oxford University Press, Inc

You, Minmin, Zude Lin, Xiuyan Li, & Jingquan Liu. 2020. "Chip-Scale Silicon Ring Resonators for Cryogenic Temperature Sensing." *Journal of Lightwave Technology* 38(20):5768–73. doi: 10.1109/JLT.2020.3002552.

Zhang, Xugang, & Xiaochun Li. 2008. "Design, Fabrication and Characterization of Optical Microring Sensors on Metal Substrates." *Journal of Micromechanics and Microengineering* 18(1). doi: 10.1088/0960-1317/18/1/015025.

Zhu, Xiantao, Minmin You, Zude Lin, Bin Yang, & Jingquan Liu. 2023. "Self-Referenced Temperature Sensors Based on Cascaded Silicon Ring Resonator."

Pp. 929–32 in *Proceedings of the IEEE International Conference on Micro Electro Mechanical Systems (MEMS).* Vols. 2023-January. Institute of Electrical and Electronics Engineers Inc. doi: 10.1109/MEMS49605.2023.10052234